

Supplementary information

Accelerated discovery of CO₂ electrocatalysts using active machine learning

In the format provided by the authors and unedited

Miao Zhong, Kevin Tran, Yimeng Min, Chuanhao Wang, Ziyun Wang, Cao-Thang Dinh, Phil De Luna, Zongqian Yu, Armin Sedighian Rasouli, Peter Brodersen, Song Sun, Oleksandr Voznyy, Chih-Shan Tan, Mikhail Askerka, Fanglin Che, Min Liu, Ali Seifitokaldani, Yuanjie Pang, Shen-Chuan Lo, Alexander Ip, Zachary Ulissi  & Edward H. Sargent 

Accelerated Discovery of CO₂ Electrocatalysts using Active Machine Learning

Miao Zhong^{†,1,2}, Kevin Tran^{†,3}, Yimeng Min^{†,1}, Chuanhao Wang^{†,1}, Ziyun Wang¹, Cao-Thang Dinh¹, Phil De Luna⁴, Zongqian Yu³, Armin Sedighian Rasouli¹, Peter Brodersen⁵, Song Sun⁶, Oleksandr Voznyy¹, Chih-Shan Tan¹, Mikhail Askerka¹, Fanglin Che¹, Min Liu¹, Ali Seifitokaldani¹, Yuanjie Pang¹, Shen-Chuan Lo⁷, Alexander Ip¹, Zachary Ulissi^{,3}, Edward H. Sargent^{*,1}*

¹Department of Electrical and Computer Engineering, University of Toronto, 10 King's College Road, Toronto, ON, Canada, M5S 3G4.

²College of Engineering and Applied Sciences, National Laboratory of Solid State Microstructures, Collaborative Innovation Center of Advanced Microstructure, Nanjing University, Nanjing 210093, China

³Chemical Engineering, Carnegie Mellon University, Pittsburgh, Pennsylvania, USA.

⁴Materials Science Engineering, University of Toronto, 200 College Street, Toronto, ON, Canada, M5S 3E5

⁵Ontario Centre for Characterization of Advanced Materials (OCCAM), University of Toronto, 200 College Street, Toronto, ON, Canada, M5S 3E5

⁶National Synchrotron Radiation Laboratory, University of Science and Technology of China, Hefei, China, 230029.

⁷Industrial Technology Research Institute, Material and Chemical Research Laboratories, Hsinchu, Taiwan, 31040.

[†] These authors contributed equally to this work.

(*) Correspondence and requests for materials should be addressed to Edward H. Sargent (ted.sargent@utoronto.ca) and Zachary Ulissi (zulissi@andrew.cmu.edu).

METHODS

DFT/ML screening methods

The automated DFT framework was constructed using various Python and shell software packages. The Materials Project^{S1} was used to establish bulk structures; the Atomic Simulation Environment^{S2} was used to manage the structures; pymatgen^{S3} was used to enumerate all facets with Miller indices between -2 and 2 and all symmetrically distinct facet terminations; pymatgen was also used to perform Delaunay triangulation on the surfaces to enumerate adsorption sites; and VASP^{S4-S7} was used to perform the DFT calculations. Each surface/site enumeration, DFT calculation, and various administrative computational tasks were encoded as interdependent tasks so that they could be managed automatically by dependency management software, Luigi^{S8}. FireWorks^{S9} was also used to manage calculations across several computing clusters. DFT results were then used by a machine learning workflow to predict CO adsorption energies for each adsorption site enumerated. To accomplish this, a method was developed to encode each adsorption site into a numerical array (Supplementary Information Fig. 1). Each element present in the bulk structure was tabulated. Each element was described with a vector four numbers: the atomic number (Z), the Pauling electronegativity (χ), the number of atoms of that element coordinated with the CO molecule (CN) as determined by a cut-off radius of 5 Å and a Voronoi polyhedral angle cutoff tolerance of 0.8,^{S3} and the median monometallic adsorption energy of CO on that element ($\Delta\widetilde{E}$) as calculated from our database of results. The vector creation process was then repeated on the “second shell” of atoms. Given that our database

included alloys with no more than three components, the final number of features was $4 \times 2 \times 3$. These features were fed to an automated machine learning tool, TPOT^{S10}, which automatically chose and tuned an appropriate regression method (typically a combination of random forest and boosted tree regressors). The chemical accuracy of Density Function Theory is about 0.1 eV. When the size of training set is smaller than 6000, the prediction error oscillates in a wide range. With the size of training set further increases, the prediction error becomes relatively stable. After using 90/10 spiting and the Random Forest Regression Algorithm, the MAE of the models we created with TPOT were *ca.* 0.18 eV and *ca.* 0.29 eV using time-series splitting. The median absolute deviation (MAD) is about 0.1eV respectively. To further improve our predictor's performance by using an extra tree regressor with 5-fold cross-validation and 95/5 splitting, both the MAD and MAE decrease to about 0.1 eV. Which is very close to the DFT accuracy. The size of our DFT data is 19644 for ΔECO .

The resulting ML model and DFT framework were then coupled to create an active machine learning workflow. The ML model was used to predict all the adsorption energies of every adsorption site enumerated by the DFT framework. The sites whose ML-predicted adsorption energies were closest to the optimal value of -0.6 eV were then automatically simulated by the DFT framework to yield a DFT-predicted adsorption energy. The additional DFT data was then used to retrain a new ML model, which created new predictions and prioritizations. Thus, the ML model used the DFT framework to query its own training data continuously, resulting in a database of DFT data that grew automatically and systematically. In total, the active learning workflow

performed over 300 ML regressions to guide DFT calculations of CO binding energies on *ca.* 4,000 different adsorption sites on Cu-containing surfaces, and *ca.* 1,000 of those were performed on CuAl surfaces.

DFT settings for screening.

We performed all DFT screening calculations using the Vienna Ab initio Simulation Package (VASP)^{S4-S7} implemented in ASE.^{S2} The RPBE functionals^{S11} were used along with k-point grids of $4 \times 4 \times 1$ and an energy cutoff 350 eV. The default pseudopotentials supplied by VASP version 5.4 were also used. Bulk relaxations were performed with a $10 \times 10 \times 10$ k-point grid and a 500 eV cutoff, and only isotropic relaxation was allowed. All surfaces were replicated in the X/Y directions so that each cell vector was at least 4.5 Å. Corrections for spin magnetism or dispersion were not included, so we excluded from this study all materials that contained Mn, Fe, Ni, Co, or O. All slabs were replicated in the Z direction to a minimum height of 7 Å with at least 20 Å of vacuum between slabs. Generally, the bottom layers were fixed and defined as those atoms more than 3 Å from the top of the surface.

Calculating the optimal ΔE_{CO} value

The literature-sourced scaling relationships^{S13} calculate an optimal adsorption free energy of CO (ΔG_{CO}) of -0.17 eV. This value was based on microkinetic modeling of the full reaction pathway from CO₂ to methane on single metal terrace (111) and step (211) surfaces and kinetic/thermodynamic scaling relationships. For Cu, hydrogenation of CO was predicted to be the rate-limiting step. If we assume that CO is still involved in the rate-limiting step of other hydrocarbon formation reactions, such as CO-CO or

HCO-HCO coupling, then similar ΔG_{CO} targets should apply. If we do not make this assumption, then the ΔG_{CO} target becomes a necessary-but-not-sufficient criterion of activity, because we still know that CO will be an intermediate in the CO₂ reduction pathway and will therefore need to have a quasi-stable ΔG_{CO} of *ca.* -0.17 eV. Thus, we need a way to calculate ΔG_{CO} .

Equation 1 can be used to calculate the change in chemical potential (ΔG_{CO})^{S13}. $\Delta\mu_{CO*}$ is the chemical potential of CO bound on a surface, $\Delta\mu_*$ is the chemical potential of the surface, and $\Delta\mu_{CO}$ is the chemical potential of CO in the gas phase.

$$\Delta G_{CO} = \mu_{CO*} - \mu_* - \mu_{CO} \quad (1)$$

Chemical potentials can be calculated using Equation 2^{S12,S13}, where E is the electronic energy as calculated by density functional theory (DFT), ZPE is the zero-point energy, C_p is the heat capacity, T is temperature, S is entropy, $\Delta\mu_{solv}$ is the change in chemical potential from solvent de-stabilization, and $\Delta\mu_{corr}$ is any experimental offset required to account for differences between experimental chemical potentials and DFT-based chemical potentials.

$$\mu = E + ZPE + \int C_p dT - TS + \Delta\mu_{solv} + \Delta\mu_{corr} \quad (2)$$

Literature^{S14} reports that ZPE_{CO} is 0.130 eV, $C_{p,CO}dT$ is 0.091 eV at 298 K, S_{CO} is 0.002092 eV K⁻¹, and $\Delta\mu_{corr,CO}$ is 0.02 eV for gas phase CO^{S14}. Thus, the chemical potential of CO in the gas phase is:

$$\begin{aligned} \mu_{CO,g} &= E_{CO,g} + ZPE_{CO,g} + \int C_{p,g} dT - TS_{CO,g} + \Delta\mu_{solv,g} + \Delta\mu_{corr,g} \\ \mu_{CO,g} &= E_{CO,g} + 0.130 \text{ eV} + 0.091 \text{ eV} + (298 \times 0.002092) \text{ eV} + 0.02 \text{ eV} \\ \mu_{CO,g} &= E_{CO,g} - 0.362 \text{ eV} \end{aligned} \quad (3)$$

The same method is used to calculate the adsorbed-state chemical potential of CO (μ_{CO*}), given literature values^{S14} for ZPE , C_p , and S as well as a solvation correction term^{S13} (μ_{solv}) and an empirical correction term^{S15} (μ_{corr}) as shown in Equation 4. Note that we assumed a CO stretch frequency of 2,000 cm⁻¹, and deviations from this frequency may cause errors.

$$\begin{aligned}\mu_{CO*} &= E_{CO*} + ZPE_{CO*} + \int C_p dT - TS_{CO*} + \Delta\mu_{solv} + \Delta\mu_{corr} \\ \mu_{CO*} &= E_{CO*} + 0.192 \text{ eV} + 0.085 \text{ eV} + (298 \times 0.000452) \text{ eV} - 0.2 \text{ eV} + 0.2 \text{ eV} \\ \mu_{CO*} &= E_{CO*} + 0.142 \text{ eV} \quad (4)\end{aligned}$$

Assuming that μ_* is equal to E_* . By combining Equations 1, 3, and 4, we can calculate the change in chemical potential of adsorbing CO:

$$\begin{aligned}\Delta G_{CO} &= \mu_{CO*} - \mu_* - \mu_{CO} \\ \Delta G_{CO} &= [E_{CO*} + 0.142 \text{ eV}] - E_* - [E_{CO,g} - 0.362 \text{ eV}] \\ \Delta G_{CO} &= E_{CO*} - E_* - E_{CO,g} + 0.50 \text{ eV} \\ \Delta G_{CO} &= \Delta E_{CO} + 0.50 \text{ eV} \quad (5)\end{aligned}$$

where the change in electronic energy, ΔE_{CO} , is defined using Equation 6 and is calculated with DFT^{S12}.

$$\Delta E_{CO} = E_{CO*} - E_* - E_{CO,g} \quad (6)$$

We combined Equation 5 with the scaling relationship's optimal ΔG_{CO} value of -0.17 eV to calculate an optimal ΔE_{CO} value of -0.67 eV. Note that we used RPBE^{S11} while the source of the scaling relationships used the BEEF-vdW^{S16} functionals though, so any differences that may be caused by using different functionals may impart errors into our estimates of activity.

Method for creating 2-dimensional activity & selectivity volcanos

We thank Xinyan Liu for providing us the code that she used to create the 2-dimensional activity map in her manuscript^{S13} to generate Fig. 1a and Supplementary Information Figure 3. to visualize our DFT/ML predicted results. The code combines adsorption energy scaling relationships with microkinetics of elementary reactions for both CO₂ reduction and H₂ evolution to predict adsorbate coverages, reaction rates, and thus activity and selectivity for CO₂ reduction vs. H₂ evolution. Additional details can be found in the Supplementary Information of Liu *et al.*^{S13}. Note that we set the scaling between H and CH_X such that they would be linearly independent; we did this to address convergence issues with the microkinetic models. Refer to Supplementary Information Figure 3 for additional results from the microkinetic modeling.

Method for creating t-SNE diagrams

To represent each adsorption site numerically, we developed two vectors: a coordination vector and a neighbours' coordination vector. Supplementary Information Fig. 2 illustrates a simplified example of these vectors. The coordination vector contains one item for each of the 31 elements considered in the screening^{S17}, and each item in this vector is the sum of the number of atoms of that element that are coordinated with CO. The neighbours' coordination vector is a flattened array contains 31×31 items for each elemental pairing, and each item in this vector is the sum of the number of atoms of one element that are coordinated with the all adsorbate neighbours that belong to another element. Algorithm 1 outlines explicitly how we calculated the neighbours' coordination number (*ncn*).

Algorithm 1 Calculating array of neighbours' coordination numbers for an adsorption site

1: $ncn := \text{zeros}(n, n)$, where $n=31$, the total number of elements we are investigating

2: **for** all neighbours **do**

3: $i :=$ index of the element of neighbour

4: **for** all neighbour's neighbours **do**

5: $j :=$ index of the element of neighbour's neighbour

6: $ncn_{i,j} := ncn_{i,j} + 1$

The coordination vector and the neighbors' coordination vector were then concatenated into one vector, scaled such that each item in the new vector had a mean of zero and a variance of one, and then sent through SKLearn's^{S18} principle component analyzer where the dimensionality was reduced until only 85% of the variance was accounted for, yielding a vector of 113 items instead of 31×32 items. This reduced vector was processed by the t-SNE algorithm^{S19} with a perplexity of 120 and a learning rate of (ϵ) of 200 and then stopped after 2,000 iterations, yielding a 2-dimensional reduction of the adsorption sites that our workflow performed DFT calculations for.

DFT calculations. The DFT calculations were performed using a VASP package in the Generalized Gradient Framework formulated by Perdew *et al*^{S23}, including the RPBE flavour of DFT and the projector augmented wave (PAW) method to account for core-valence interactions^{S20-S23}. The cutoff of kinetic energy for plane wave expansions was set to 400 eV and the reciprocal space was sampled by the Γ - centred Monkhorst–Pack scheme^{S25} with a grid of $4 \times 4 \times 1$ and an energy cutoff 350 eV. The Cu (111) and (100) surface slabs were constructed with three Cu layers using ASE (Atomic Simulation

Environment)^{S24} using the RPBE-optimized lattice parameter with a vacuum layer of at least 15 Å.

Zero-point energies (ZPE), enthalpy and entropy contributions to free energies at room temperature (298.15 K) were calculated from vibrational modes of surface species using numerical six-point derivatives in VASP and ASE. Note that very low-frequency modes were obtained in some cases because the explicit water molecules are not properly constrained by the hydrogen bonding network presented in water bulk. Such low-frequency modes can cause unphysically large entropy contributions, so they were reset to a threshold value of 60 cm⁻¹ and excluded frequencies smaller than the threshold, corresponding to the acoustic translational mode of the six-member rings in water bulk.

For the surface reaction (i.e., $A^* \rightarrow B^*$), the change in Gibbs free energy at temperature T and 1 atmospheric pressure is given by:

$$\Delta G_{A^* \rightarrow B^*}(T, P^0) = \Delta E_{rxn} + \Delta H^0(T) - T\Delta S^0(T, P^0)$$

where ΔE_{rxn} is the calculated reaction energy of $A^* \rightarrow B^*$. $\Delta H^0(T)$ and $\Delta S^0(T, P^0)$ are the enthalpy and entropy differences between the initial and final states. In addition, $\Delta H^0(T)$ gives the zero-point energy and the temperature dependence of enthalpy change at a standard pressure of 1 atm for adsorption of molecule A (here, it is room temperature of 298.15 K), which is given by:

$$\begin{aligned}\Delta H^0(T) &= H_{trans}^A + H_{rot}^A + H_{vib}^A - H_{vib}^{A^*} \\ \Delta S^0(T) &= S_{trans}^A + S_{rot}^A + S_{vib}^A - S_{vib}^{A^*}\end{aligned}$$

where H_{trans}^A , H_{rot}^A , H_{vib}^A and $H_{vib}^{A^*}$ is the enthalpy at the temperature T and a standard pressure of 1 atm for the translational, rotational, vibrational modes of the A.

S_{trans}^A , S_{rot}^A , S_{vib}^A and $S_{vib}^{A^*}$ are entropy contributions from the 3-D translational, 2-D rotational, vibrational modes.

Preparation of evaporated Cu on gas diffusion layers (GDLs). Cu was evaporated on the GDL (Fuel Cell Store, Sigracet 39 BC) by a thermal evaporation process. GDL is made of an air-brushed polytetrafluoroethylene (PTFE) on carbon nanoparticles layer as a conductive and hydrophobic layer atop a carbon fibre layer as a conductive and supporting layer. 0.5 g Cu foils were placed in a crucible inside the evaporation chamber (Edwards AUTO 360 Thermal Evaporator). A thin Cu layer (~ 500 nm) was deposited at an evaporation rate of approximately $1\text{-}2 \text{ nm s}^{-1}$ under a base pressure of 10^{-6} Torr. GDLs were kept rotating at a slow speed of 50 rpm during evaporation.

Preparation of ion-implanted Al-on-Cu on GDLs. Evaporated Cu on GDL samples were used as substrates and placed in ion implantation chamber (50keV Aluminum Implantation at Western University). A 99.999% purity aluminium (Al) rod is installed in a copper target in the caesium (Cs) sputter source. A 100keV Al_2^- molecules are produced in the sputter source injector, selected by the injector magnet and injected into the Tandetron accelerator. Al_2^- is preferred because it has six times the flux of Al^- . For ion implants below 100keV, the Tandetron terminal pump and stripper gas are turned off. The Tandetron is used as a large lens to focus a negative beam to target in the implant chamber. The high energy magnet steers the Al_2^- down the beamline with the implant chamber. As the beam travels down the beamline it passes through NEC Electrostatic Raster/Scanner which sweeps the beam in the X direction at 517Hz and 64Hz in the Y direction over an aperture which defines the implant area on the implant

stage. The Al_2^- molecule breaks into Al each having an energy of 50keV after the collisions with the sample. The implant stage has 4 sides. Each side can be rotated to face the beam for implantation. The implant stage in the Implant Chamber is suspended in a Faraday cage to suppress the secondary electrons. The ion charge is collected from the implant stage and fed to an Ortec 439 current integrator. The charge is converted into pulses which are counted by a computer to determine the dose. To avoid substantial ion-beam induced damage and over-heating to the samples, we ion implanted 2 w% Al into Cu which corresponded to 6×10^{15} ions cm^{-2} . It took 112 minutes to finish this experiment. Auger spectroscopic analysis determined that the Al/(Al+Cu) molar concentration on the surface is ~4.5%. We implanted 5 wt% and 10 wt% Al into Cu and it took 180 and 360 minutes, respectively. Surface Al concentrations are determined to be 5% and 5.5 %, indicating making more Al on Cu surface is difficult by the ion implantation method. This may be due to the ion-beam-induced damage and heating effect. Al may gradually migrate into the bulk at a large implantation dose.

Preparation of evaporated-etched Al-on-Cu on GDLs. Evaporated-etched Al-on-Cu was synthesized via a two-step process of evaporation and etching. First, 0.3 g Al foils were placed in a crucible inside the evaporation chamber. A thin Al layer (~ 100 nm) was deposited on evaporated Cu-on-GDL samples at an evaporation rate of approximately $1\text{-}2 \text{ nm s}^{-1}$ under a base pressure of 10^{-6} Torr. The evaporated Al-on-Cu sample was then immersed in a 5 wt% hydrochloric acid solution to remove the excessive Al. The solution was kept stirring at a low speed of 250 rpm during the 5

minutes etching. Deionized water was used to wash off remained hydrochloric acid and other residual ions from the sample surface. An airbrush was used to dry the samples.

Preparation of de-alloyed Cu-Al and nanoporous Cu on GDLs. De-alloyed Cu-Al was synthesized via an evaporation and etching process. First, 0.5 g Cu foils and 0.25 g Al foils were placed in a crucible inside the deposition chamber. They were melted under a base pressure of 10^{-6} Torr for 2 minutes to form greyish Cu-Al alloys. Then, a thin layer of Cu-Al alloy (~ 500 nm) was deposited on GDLs at an evaporation rate of approximately $1\text{-}2 \text{ nm s}^{-1}$ under a base pressure of 10^{-6} Torr. After cooling down to room temperature naturally, the evaporated Cu-Al alloy on GDL samples were transferred to a 5 wt% hydrochloric acid solution to fabricate de-alloyed Cu-Al catalyst at a mild stirring speed of 250 rpm. Deionized water was used to wash off remained hydrochloric acid and other residual ions from the sample surface. An airbrush was used to carefully dry the samples.

Nanoporous Cu samples were prepared by immersing de-alloyed Cu-Al catalysts into 10 mM CuCl₂ solution for 10 minutes with a mild stirring speed of 50 rpm. Then, the samples were washed with deionized water and dried by an airbrush carefully.

Preparation of de-alloyed Cu-Al on polytetrafluoroethylene (PTFE) substrates. De-alloyed Cu-Al was fabricated on the PTFE (pore size: 0.45 μm) substrates via a co-sputtering and etching process. To avoid melting of PTFE at high temperatures during evaporation, co-sputtering was used. First, a 200 nm thick Cu-Al layer was co-sputtered on the PTFE using a Cu target (99.99%) and an Al target (99.99%) at a sputtering rate of 3.1 \AA/s and 1.1 \AA/s respectively under a base pressure of 10^{-6} Torr. Following the

chemical etching process in a 5 wt% hydrochloric acid solution, the co-sputtered Cu-Al was de-alloyed to prepare the high-performance de-alloyed Cu-Al. The remained hydrochloric acid and residual ions on the surface was washed off by deionized water. The samples were then carefully dried with an air gun. For the stability test, carbon black nanoparticles (Sigma-Aldrich, < 100 nm) and graphite were dispersed in a mixture of isopropanol, water and Nafion solution (50 microliter of Nafion solution in 0.5 mL of isopropanol:water mixture)³. The mixture was sonicated for 1 hour and then spray coated on the Cu-Al/PTFE electrodes.

Characterizations. The morphologies of the prepared samples were investigated using scanning electron microscope (SEM) on a Hitachi SU 5000 VPSEM, transmission electron microscope (TEM) on a Hitachi HF-3300 instrument with an acceleration voltage of 200 kV and high-angle annular dark-field scanning transmission electron microscopy (HAADF-STEM) in a Cs-corrected STEM (JEOL, JEM-ARM200F) at an accelerating voltage of 200 kV. Compositions of the prepared samples were studied using Energy-dispersive X-ray spectroscopy (EDX) on a Bruker Quantax EDX in SEM and TEM, respectively, and electron energy loss spectroscopy (EELS) elemental analysis by GIF Quantum 965. Al concentrations on surfaces of the prepared samples were measured using Auger electron spectroscopy (AES) on a 710 Scanning Auger Nanoprobe instrument (Ulvac-PHI, Chigasaki, Japan). The beam settings used for the acquisition are 10keV and 10nA. We performed AES analyses at different locations on the surface for each sample to trace the Al concentrations and homogeneity. We found that ion implantation gave rather uniform distributions of Al on the surfaces. In contrast,

Al concentrations on those chemical etched samples may vary \pm 5-10% especially for those samples with high Al concentrations, indicating that the chemical etching condition using HCl solutions might be further optimized. The Cu and Al ion concentrations in the testing solutions were measured using an Inductively Coupled Plasma Atomic Emission Spectrometer (ICP-AES Agilent Dual-View 720 with CCD for full wavelength coverage between 167 to 785 nm.). Note that KOH concentration in the catholyte is high which causes ICP_AES flame extinction during analysis so that we need to dilute the KOH catholyte 100 times for the 1 M KOH solution and corresponding 300 times for the 3 M KOH + 3 M KI solution. Thus, the detected Cu and Al impurities in the catholytes are in the ppb range for both Cu and Al in the diluted solutions, which is close to the detection limit of 2.4 ppb for Cu and 1.3 ppb for Al in our ICP-AES spectroscopy.

Ex situ and *in situ* X-ray absorption spectra at Cu K-edge on catalysts and standard references were collected at the beamline of 1W1B from Beijing synchrotron radiation facility, China. The electron storage ring was operated at 2.5 GeV with an average current of 200 mA. A Si (111) double crystal was used as a monochromator and the data of absorption were collected in fluorescence mode. The energy of the absorption spectra was calibrated by measuring the X-ray absorption near edge spectroscopy (XANES) of a Cu metal foil. The obtained data were processed by established methods with the ATHENA software package. The normalized Extended X-ray absorption fine-structure spectroscopy (EXAFS) was converted from energy to k -space and weighted by k^3 . These data were then Fourier transformed to R-space.

For *in situ* measurements, a self-built flow cell consisting of two chambers for CO₂ diffusion (chamber I) and holding the reaction liquid (chamber II) was used. The sample is sandwiched between the two chambers with pressed the Teflon spacers (sample size: 1.2 × 1.2 cm²; thickness: ~500 nm). CO₂ gas is introduced into the chamber I with the gas controller and diffuses and passes through the samples and finally reaches the liquid to participate in the reaction. The thickness of the liquid can be controlled from 1000 to 200 μm. After the liquid cell filled with 1.0 M aqueous KOH, 30 mL KOH solution with the same concentration is flowed into the liquid cell at 0.5 mL/min by using an automatic pump syringe. The measurement of the Cu K-edge is started simultaneously with the stop of the flowing.

The *ex situ* XANES Al K-edge spectra of the de-alloyed Cu-Al samples were collected on the 4B7B beamline at Beijing Synchrotron Radiation Facility, Beijing, China, operating at a flux of 1 × 10¹⁰ phs/s with a beam current of 100 mA. The Al K-edge XANES spectra were scanned between 1480 eV and 1800 eV in vacuum. The spectra were then calibrated to the K-edge of an Al metallic foil (1559 eV), and normalized to the maxima of the absorption spectra.

Electrochemical reduction of CO₂. All CO₂ electrolysis experiments were performed using a three-electrode set-up in a flow-cell configuration connected to an electrochemical workstation (Autolab PGSTAT302N). An Ag/AgCl (in saturated KCl solution) and a platinum wire were used as reference and counter electrodes, respectively. 1M KOH was used as the electrolyte. To quantify FEs for each product, we performed CO₂ electrolysis in a chronopotentiometry mode. For Tafel analysis, we

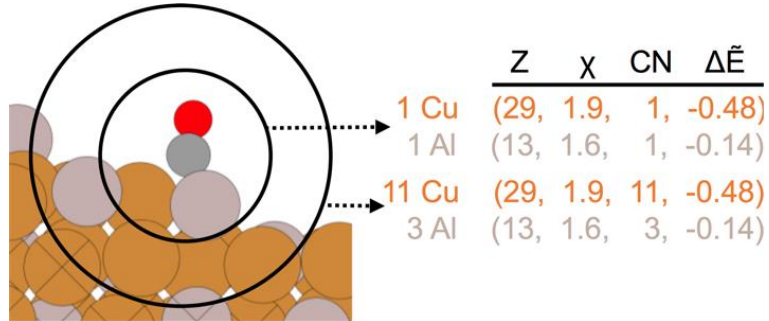
performed CO₂ electrolysis in a Chronoamperometry mode. For linear sweep voltammogram (LSV) analyses, we cycled the LSV until it was stable. For IR corrections, we measured the resistance of electrolyte and used its 90% value for IR compensation.

In our experiment, we applied the working potential between the cathode and the reference electrode before adding KOH catholyte into the cathodic chamber. We also passed a small amount (~ 3 ml which depends on the size of the cathodic chamber) of 1 M KI catholyte (pH 5.5-6.5) as a buffer electrolyte before passing the real testing KOH catholyte. In this way, the dissolution of Al into solution is avoided. The 3 ml 1 M KI was pumped out of the system after use as a buffer solution at the beginning stage of the test. We also tried 1 M KHCO₃ as a buffer solution, and the performance was the same. After finishing the experiments, we replaced the KOH catholyte with the neutral KHCO₃ electrolyte in the cathodic chamber first at an applied working potential, so that the remaining KOH on the sample surfaces was washed out. After removal of the samples from the flow cell and washing them carefully with DI water, we performed sample characterizations.

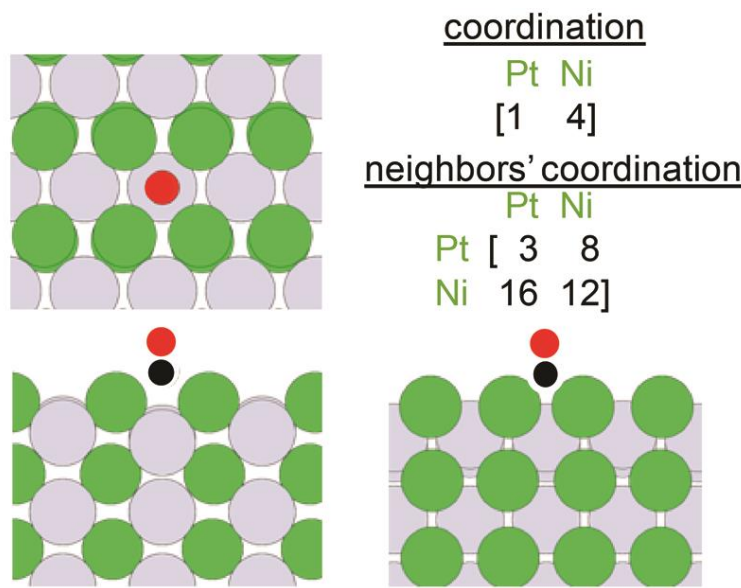
The cathodic chamber was separated from the gas chamber by a 1.5 cm × 1.5 cm gas diffusion electrode (GDE). GDEs were made of catalysts on GDLs as discussed in detail above. A plastic plate with a 1cm × 1cm window is placed between the GDE and cathode chamber. The cathodic chamber was separated from the anodic chamber by an anion exchange membrane (Fumasep FAA-3-PK-130). Rubber spacers were placed in between different chambers to avoid mixture of electrolytes or gaseous products.

CO_2 gas was delivered into the gas chamber at a rate of 56 standard cubic centimetres per minute (s.c.c.m.) and was routed into a gas chromatograph (Perkin Elmer Clarus 680) to quantify the gaseous products. The liquid products were quantified by NMR (600 MHz Agilent DD2 spectrometer), in which electrolyte was mixed with D₂O (deuterated water) and dimethyl sulfoxide (DMSO, Sigma, 99.99%) was used as an internal standard.

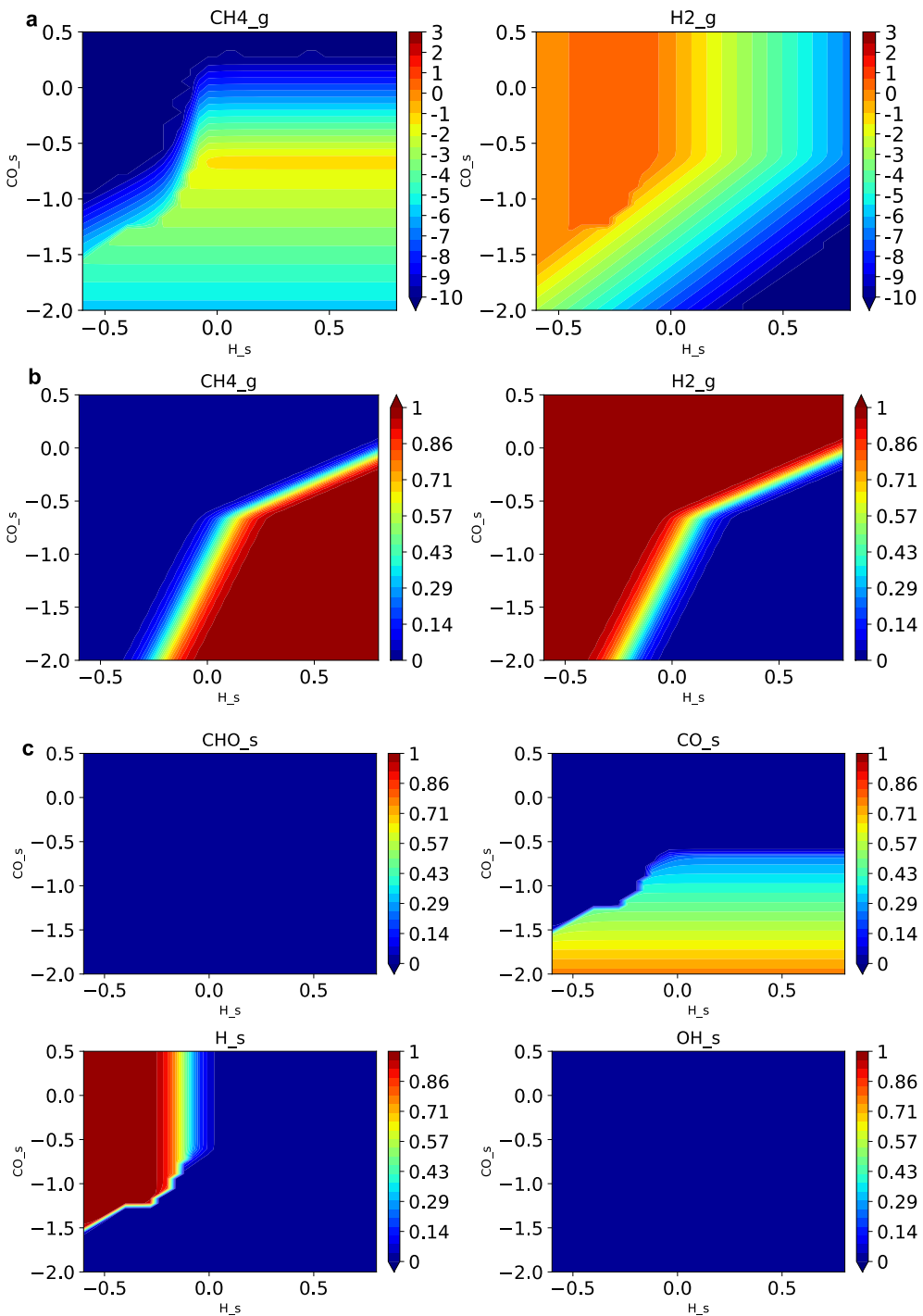
Faradaic efficiencies (FEs) for different products can be calculated as follows: $\text{FE} = \frac{\text{F} \times \text{m} \times \text{n}}{\text{Q}} = \frac{\text{F} \times \text{m} \times \text{n}}{(\text{I} \times \text{t})}$, where F is the Faraday constant, m is the electron numbers needed for one CO_2 molecule reduction to the desired product and n is the amount of the desired product (in moles). A half-cell CO_2 -to- C_2H_4 power conversion efficiency in a full-cell $\text{CO}_2 + \text{H}_2\text{O}$ -to- $\text{C}_2\text{H}_4 + \text{O}_2$ reaction (half-cell C_2H_4 PCE) can be estimated as follows: Half-cell C_2H_4 PCE = $\text{FE} \times \frac{V_{\text{theoretic}}}{V_{\text{real}}}$, where $V_{\text{theoretic}} = 1.17$ (V_{RHE}), $V_{\text{real}} = (1.23 - V_{\text{applied}}) (\text{V}_{\text{RHE}})^{\text{S28-S30}}$.



Supplementary Information Figure 1 | An example of the numerical encoding of an adsorption site. Vectors are created for each element present within the first and second neighbouring shells of CO. Each vector contains the atomic number of the element (Z), the Pauling electronegativity of the element (χ), the number of atoms of that element within each respective shell (CN), and the median monometallic adsorption energy of CO on that element ($\Delta\tilde{E}$). Color codes for elements: orange is Cu, light gray is Al, dark gray is C, and red is O.



Supplementary Information Figure 2 | A simplified example of a numerical representation of a coordination site which was used for t-SNE analysis. Each item in the “coordination” vector represents the coordination number for a particular element, e.g., Pt or Ni. Each item in the “neighbours' coordination” array represents this same coordination vector, but for each of the adsorbate's neighbours. Note that this example is for illustrative purposes only. The vectors and arrays actually used contained enough items to represent 31 different elements, totalling in 31×32 features. Color codes for elements: green is Ni, light gray is Pt, black is C, and red is O.



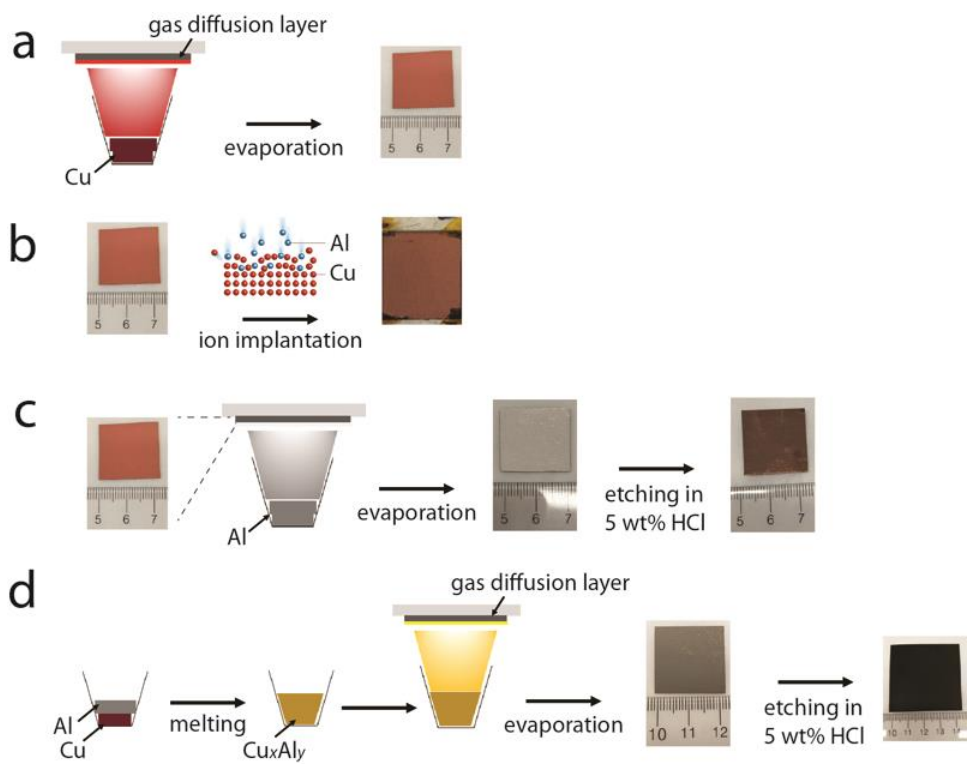
Supplementary Information Figure 3 | Activity, selectivity, and coverage maps at -0.5 V

applied potential, based on (211) metal scaling relations and microkinetic models. **a,**

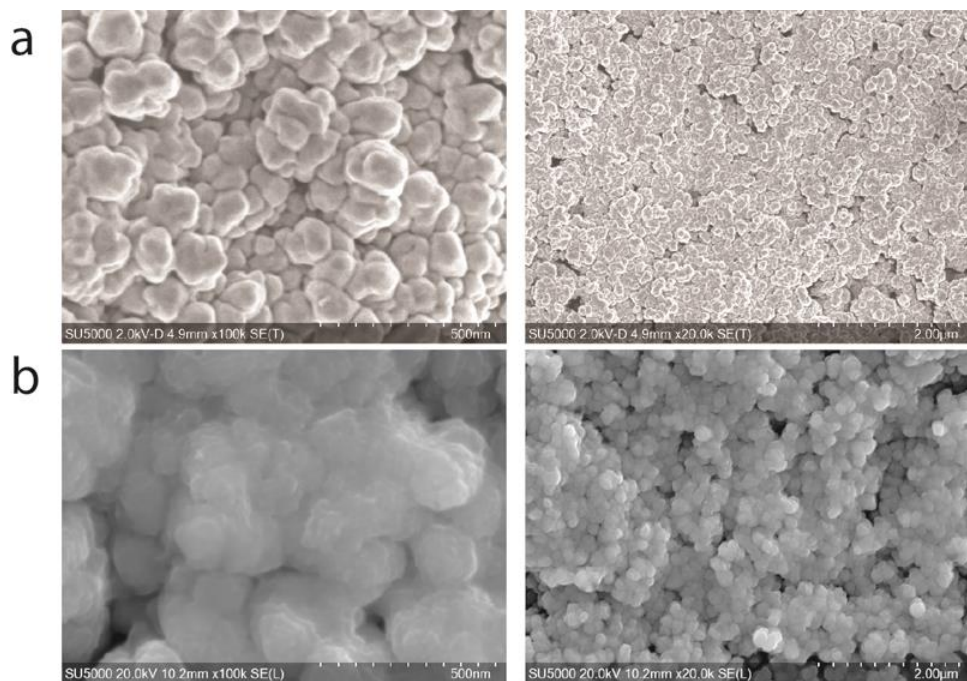
Activity of CH₄ and H₂ production (in units of log(TOF [1/s])) as a function of ΔE_{CO} vs. ΔE_H . **b,**

Selectivity towards CH₄ and H₂ production as a function of ΔE_{CO} vs. ΔE_H . **c,** Surface coverages

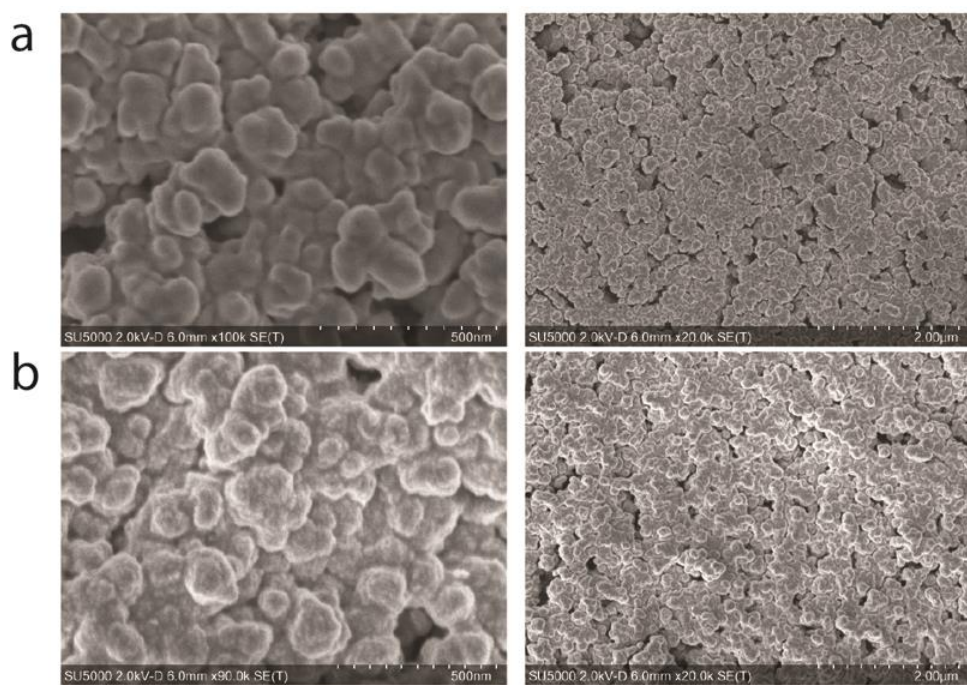
of CHO, CO, H, and OH adsorbates as a function of ΔE_{CO} vs. ΔE_H .



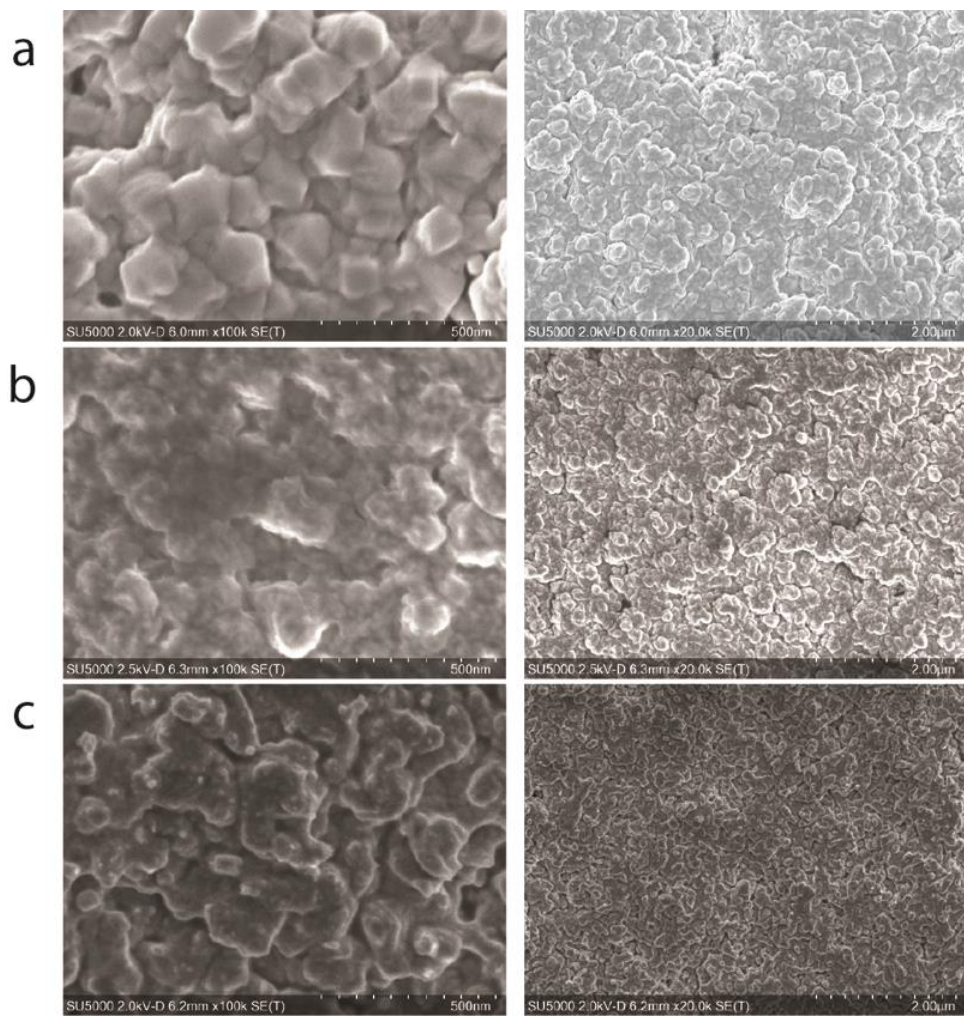
Supplementary Information Figure 4 | Schematic for the synthesis of different catalysts on gas diffusion layers. **a**, evaporated Cu. **b**, ion-implanted Al-on-Cu. **c**, evaporated-etched Al-on-Cu. **d**, de-alloyed Cu-Al catalysts.



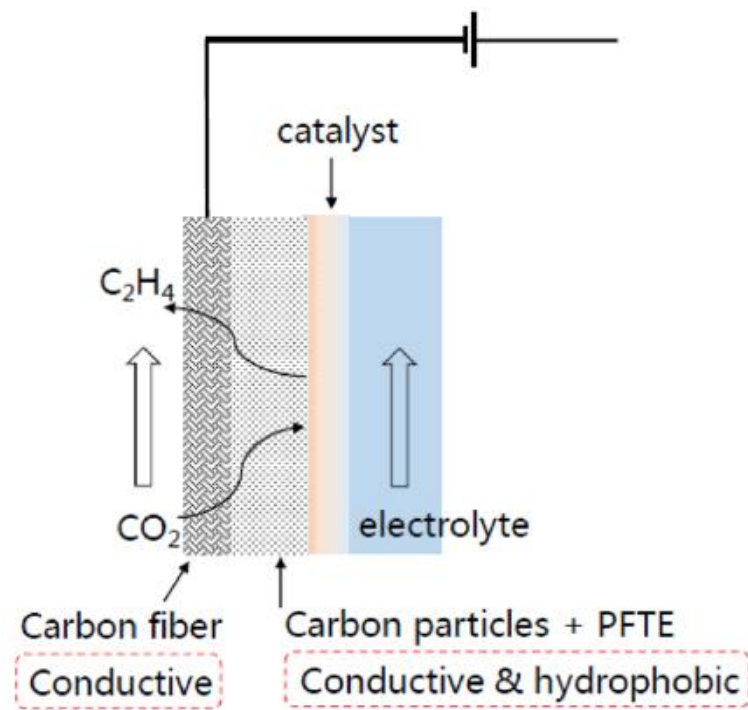
Supplementary Information Figure 5 | Morphologies of evaporated Cu catalysts on gas diffusion layers. **a**, Top-view SEM images before CO₂ electroreduction. **b**, Top-view SEM images after 5 hours CO₂ electroreduction in 1 M KOH at an applied current density of 600 mA cm⁻² in a flow cell.



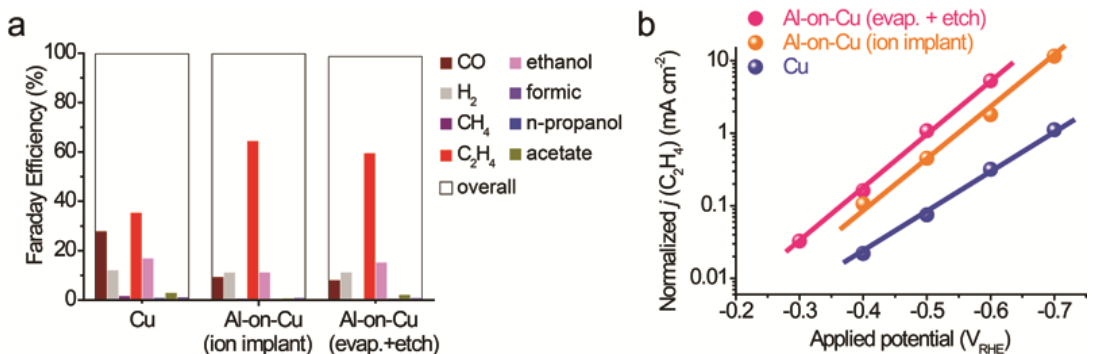
Supplementary Information Figure 6 | Morphologies of ion-implanted Al-on-Cu catalysts on gas diffusion layers. **a**, Top-view SEM images before CO_2 electroreduction. **b**, Top-view SEM images after 5 h CO_2 electroreduction in 1 M KOH at an applied current density of 600 mA cm^{-2} in a flow cell.



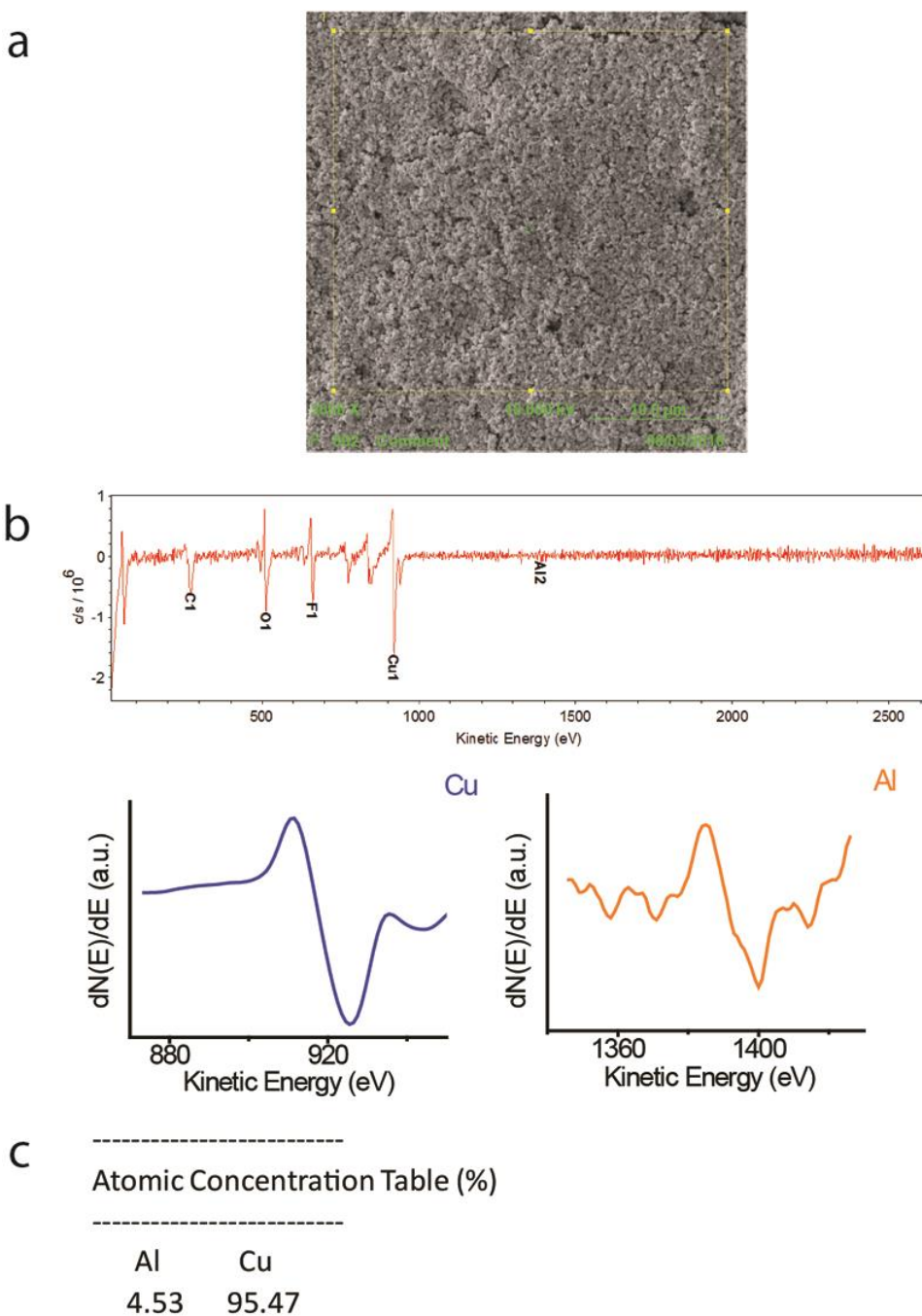
Supplementary Information Figure 7 | Morphologies of evaporated and evaporated-etched Al-on-Cu samples on gas diffusion layers. **a**, Top-view SEM images of the as-evaporated Al-on-Cu samples. **b**, Top-view SEM images of the evaporated-etched Al-on-Cu catalyst before CO_2 electroreduction. **c**, Top-view SEM images of the evaporated-etched Al-on-Cu catalyst after 5 hours CO_2 electroreduction in 1 M KOH at an applied current density of 600 mA cm^{-2} in a flow cell.



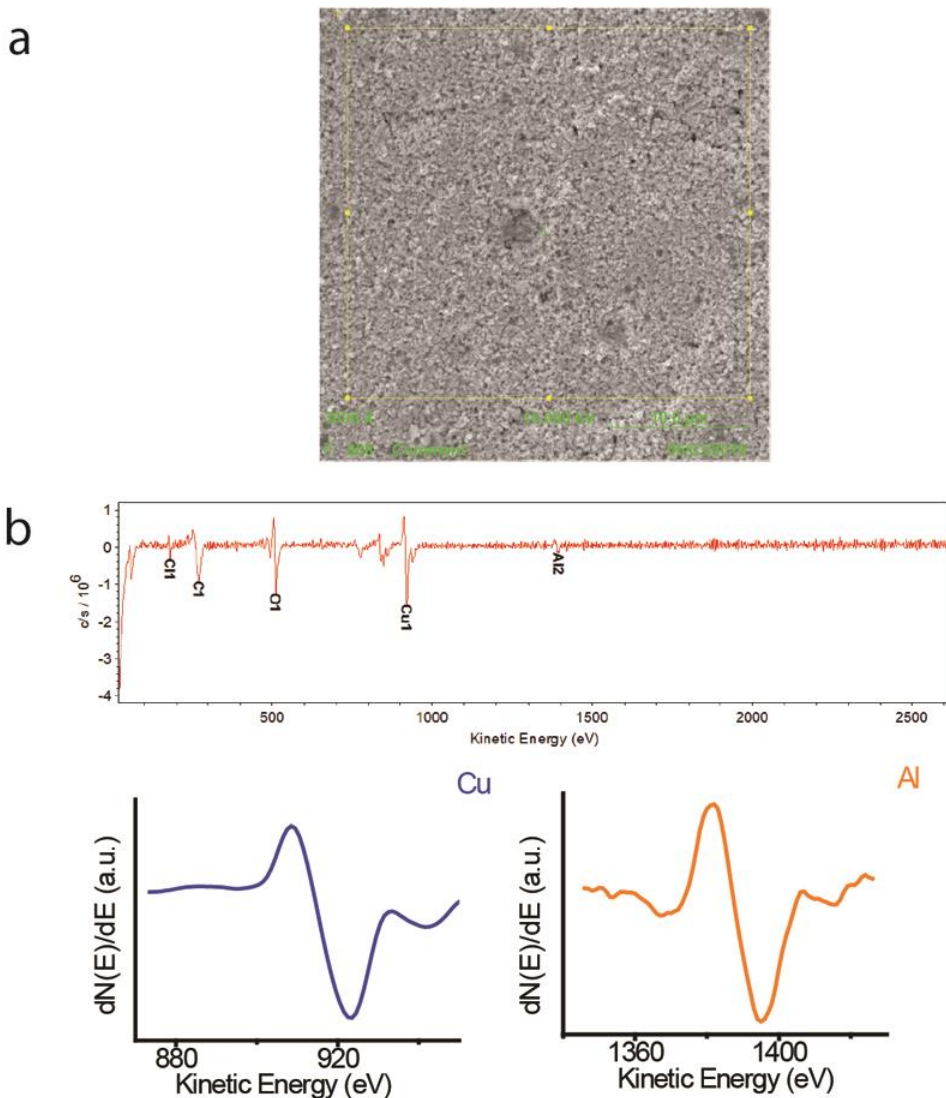
Supplementary Information Figure 8 | Schematic of the cathode side in a flow-cell configuration.



Supplementary Information Figure 9 | CO₂ electroreduction performances on pure Cu, ion-implanted Al-on-Cu, and evaporated-etched Al-on-Cu catalysts. **a**, Faradaic efficiencies of gaseous products on pure Cu, ion-implanted, and evaporated-etched Al-on-Cu obtained from chronopotentiometry tests at an applied current density of 600 mA cm⁻². **b**, C₂H₄ production partial current density versus potential on pure Cu, ion-implanted, and evaporated-etched Al-on-Cu.



Supplementary Information Figure 10 | Auger electron spectroscopic analysis of an ion-implanted Al-on-Cu catalyst. **a**, Auger secondary electron microscopic image. **b**, Auger spectroscopic survey and narrow-scan spectra. **c**, Concentrations of Cu and Al.

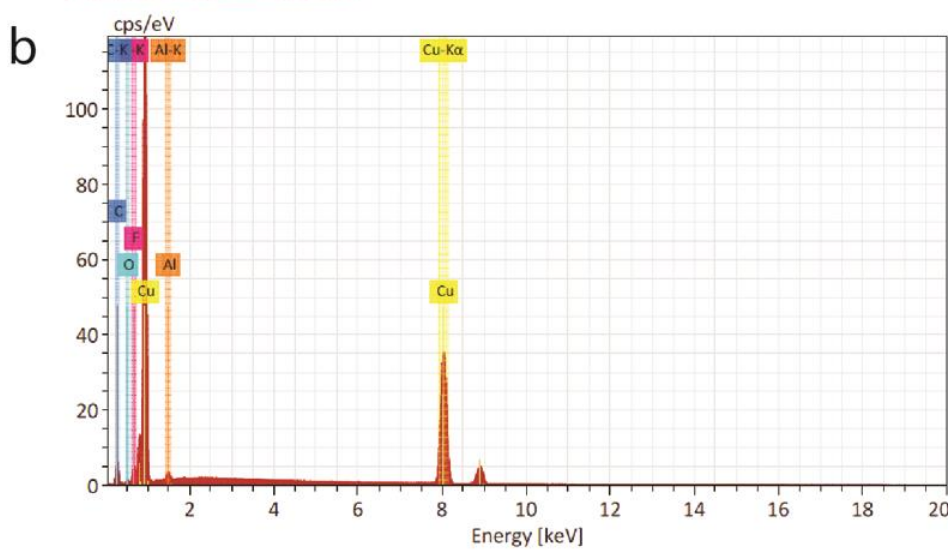
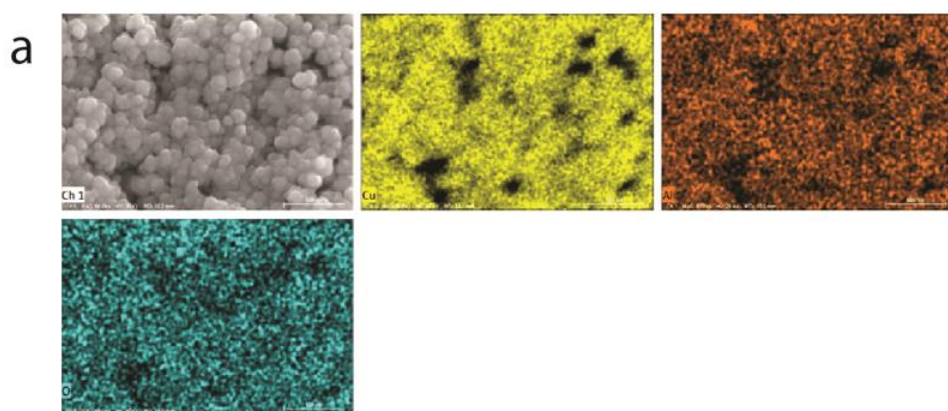


c

Atomic Concentration Table (%)

Al	Cu
24.67	75.33

Supplementary Information Figure 11 | Auger electron spectroscopic analysis of an evaporated-etched Al-on-Cu catalyst. a, Auger secondary electron microscopic image. b, Auger spectroscopic survey and narrow-scan spectra. c, Concentrations of Cu and Al.

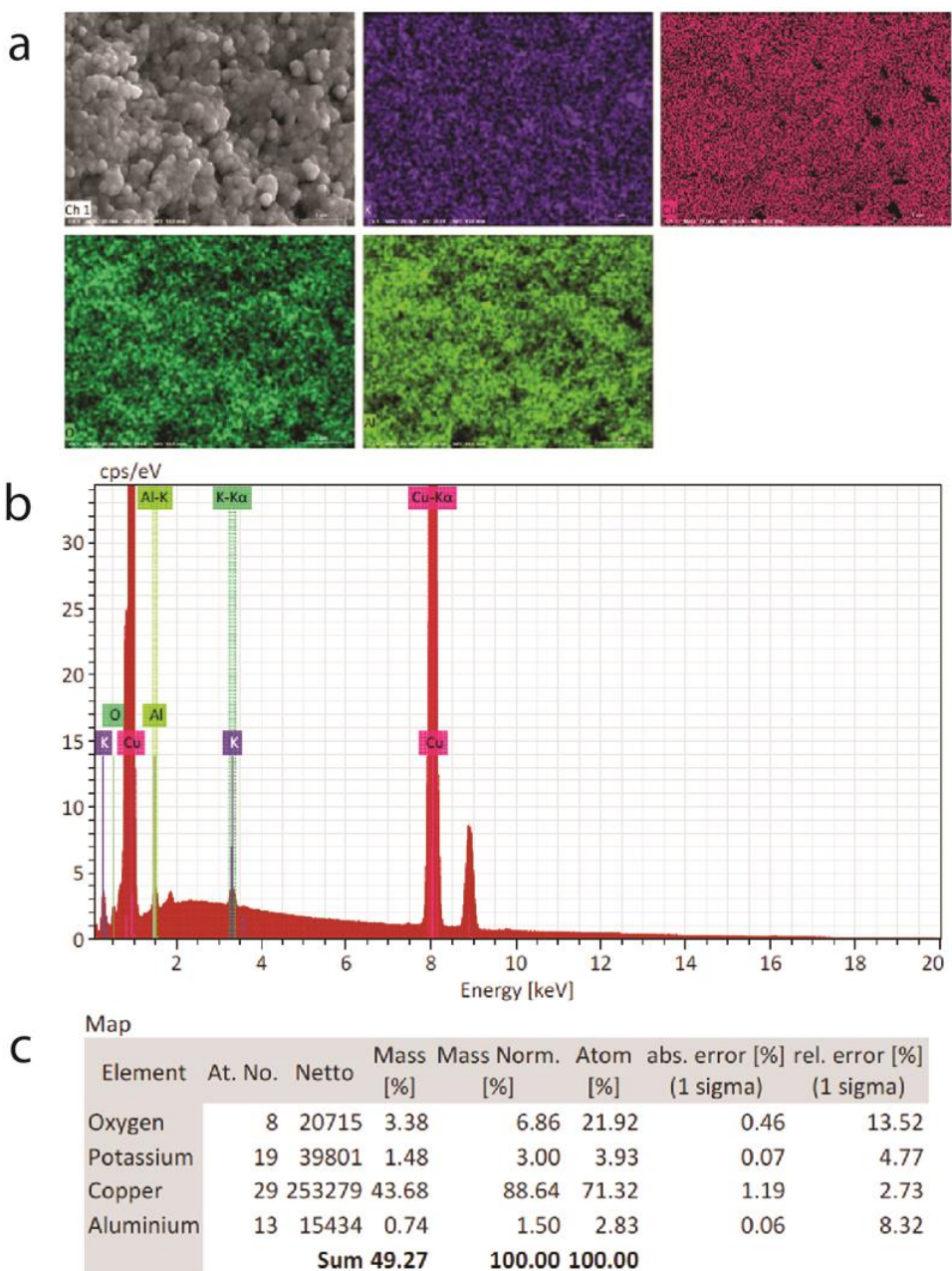


c

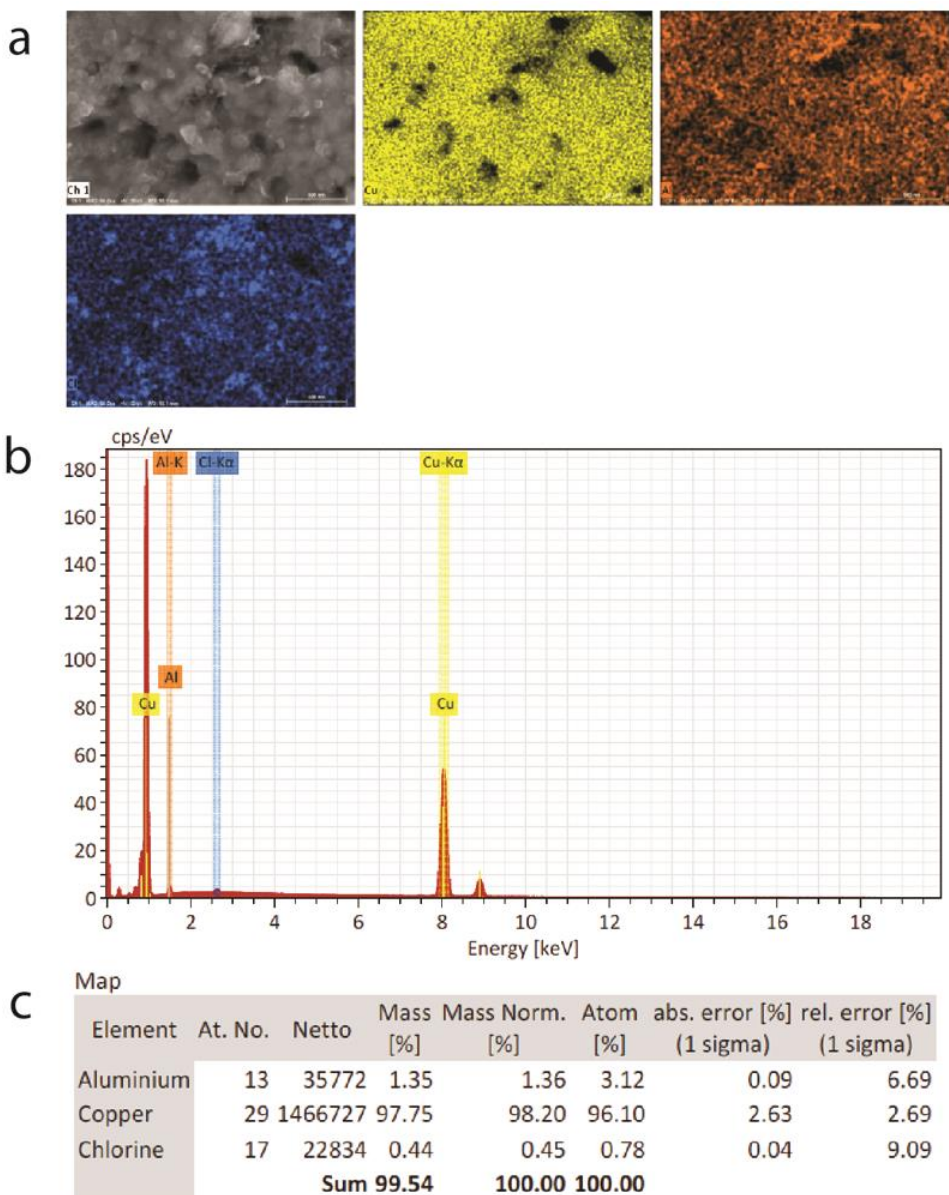
Map

Element	At. No.	Netto	Mass [%]	Mass Norm. [%]	Atom [%]	abs. error [%] (1 sigma)	rel. error [%] (1 sigma)
Aluminium	13	17053	1.54	1.52	3.44	0.10	6.54
Copper	29	463104	99.23	97.91	94.37	2.68	2.70
Oxygen	8	2983	0.58	0.57	2.19	0.13	21.64
Sum 101.34				100.00	100.00		

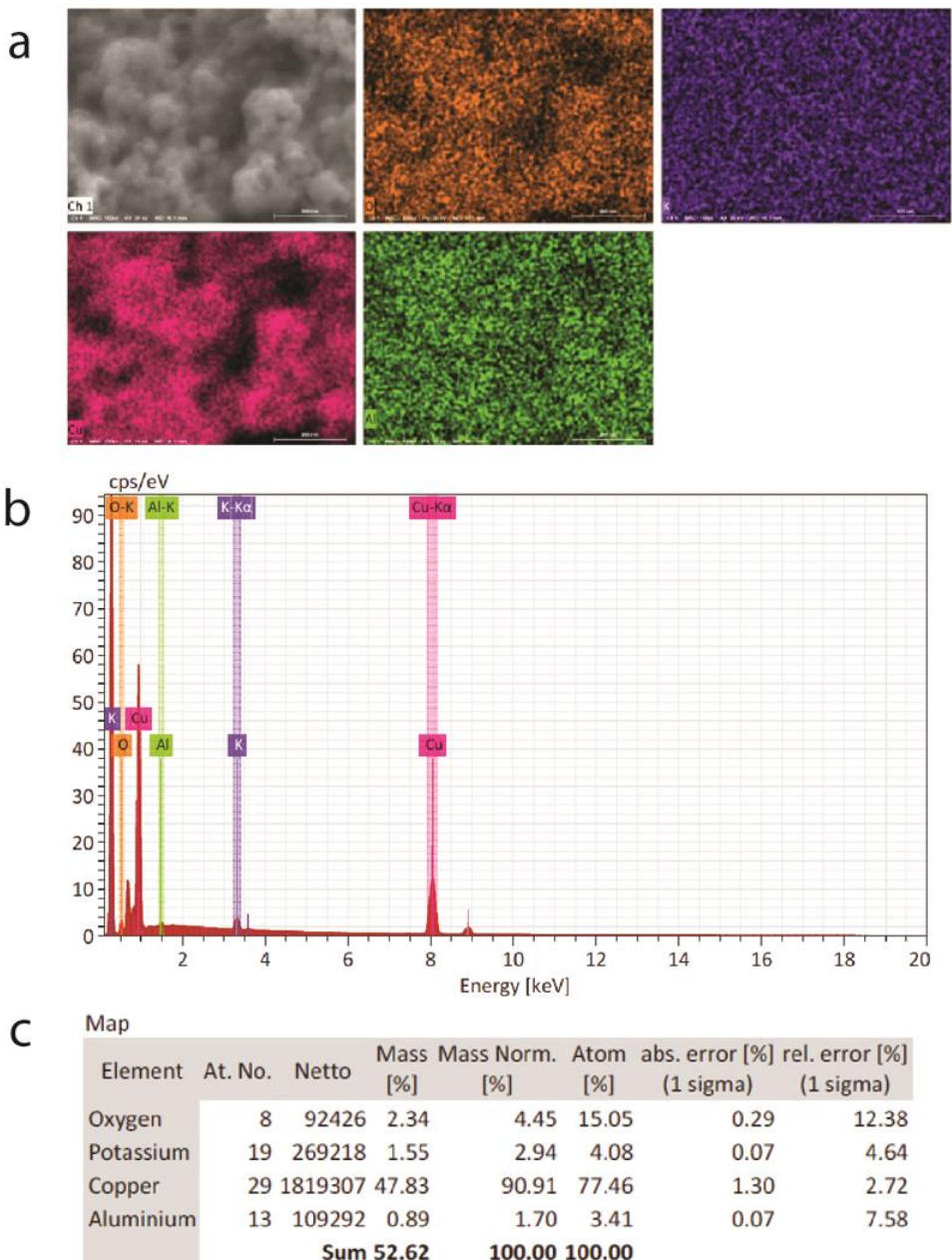
Supplementary Information Figure 12 | EDX analysis of an as-prepared ion-implanted Al-on-Cu sample before CO₂ electroreduction. a, EDX mapping. b, EDX spectrum. c, Elemental concentrations.



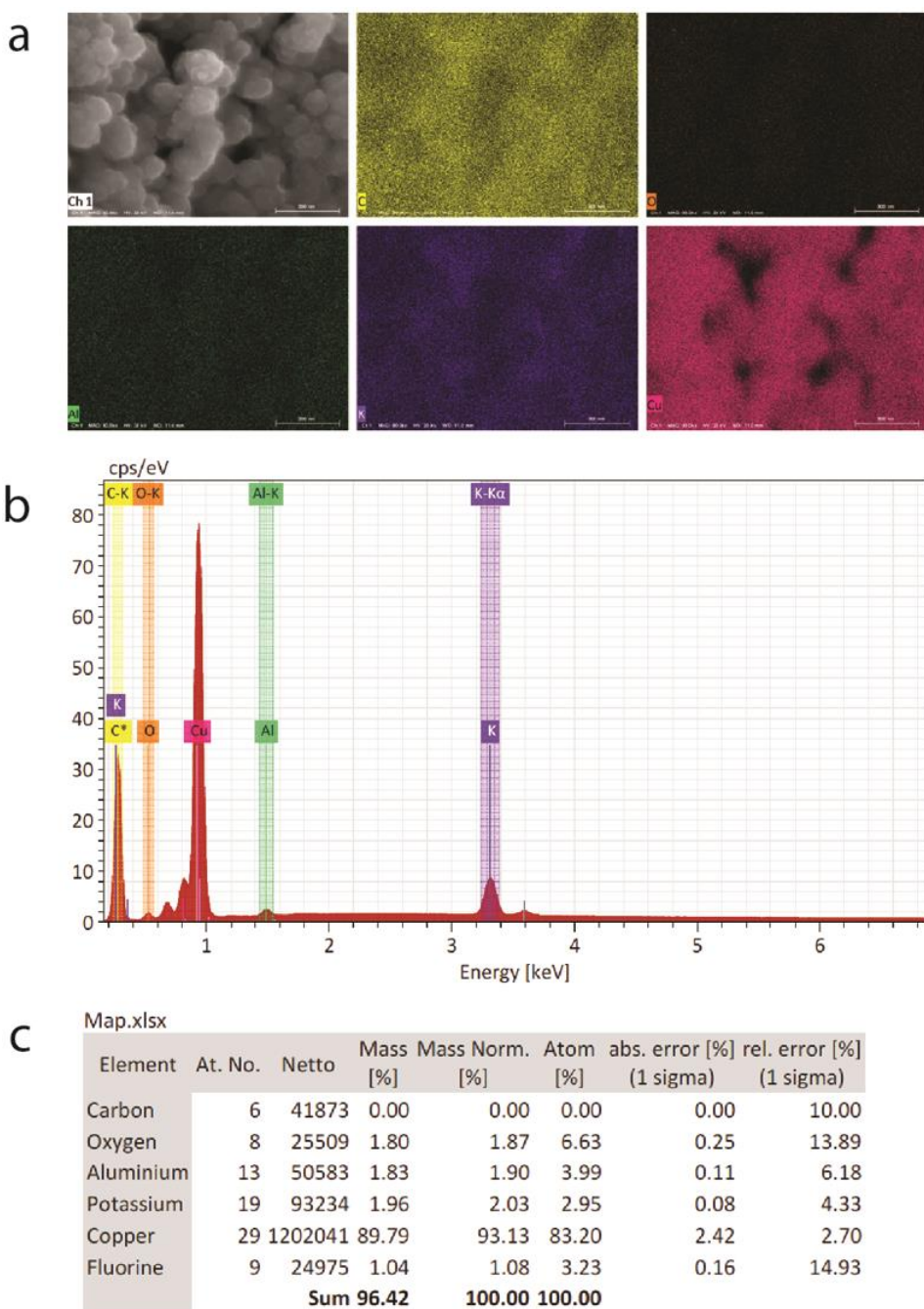
Supplementary Information Figure 13 | EDX analysis of an ion-implanted Al-on-Cu sample after 5 hours CO₂ electroreduction at 600 mA cm⁻² (-1.8 to -2.0 V_{RHE}) in the 1 M KOH electrolyte. a, EDX mapping. b, EDX spectrum. c, Elemental concentrations. Potassium is observed on the surface after the reaction.



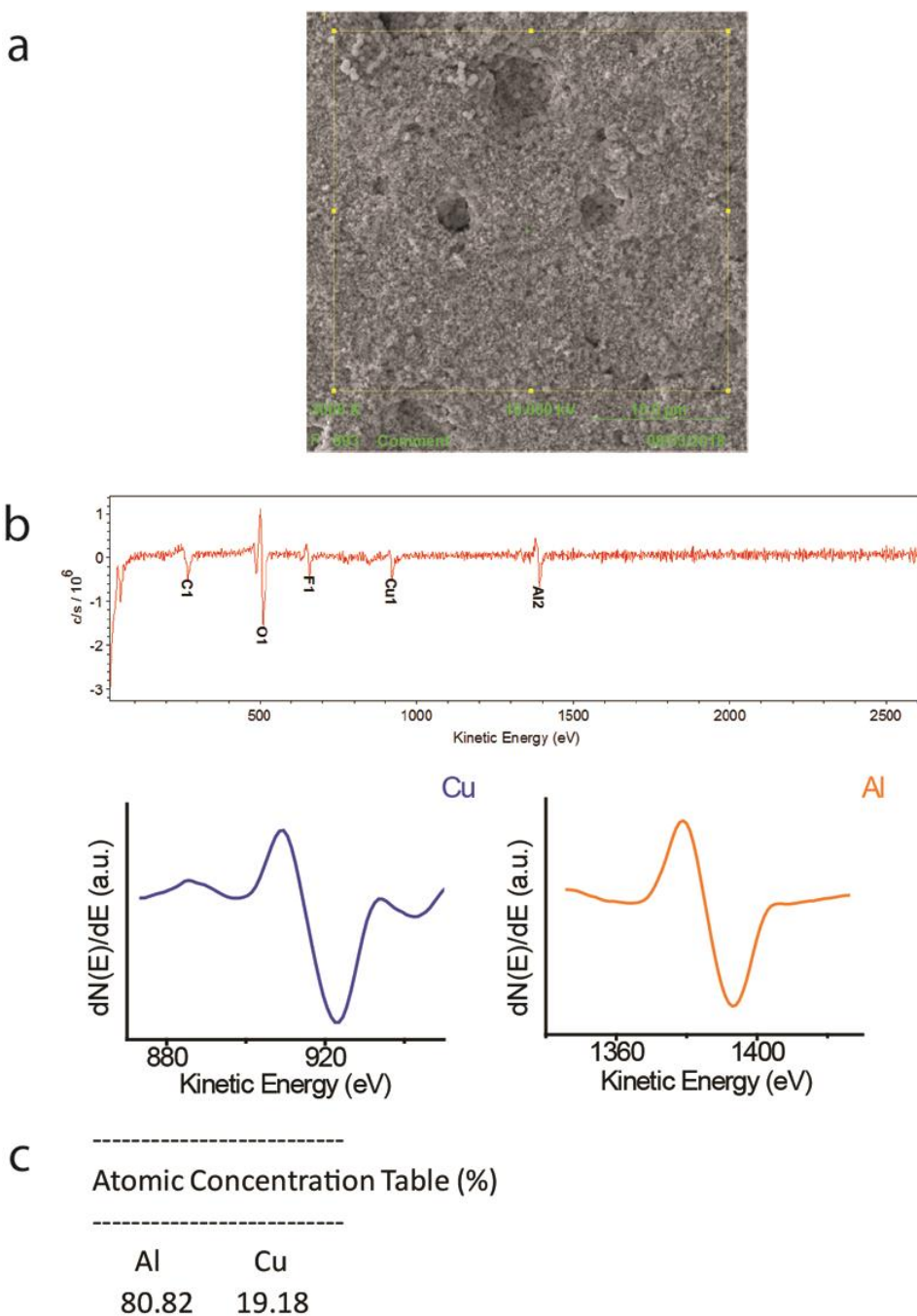
Supplementary Information Figure 14 | EDX analysis of an evaporated-etched Al-on-Cu sample before CO₂ electroreduction. **a**, EDX mapping. **b**, EDX spectrum. **c**, Elemental concentrations. Chlorine is observed on the surface due to the use of HCl solution in the etching process.



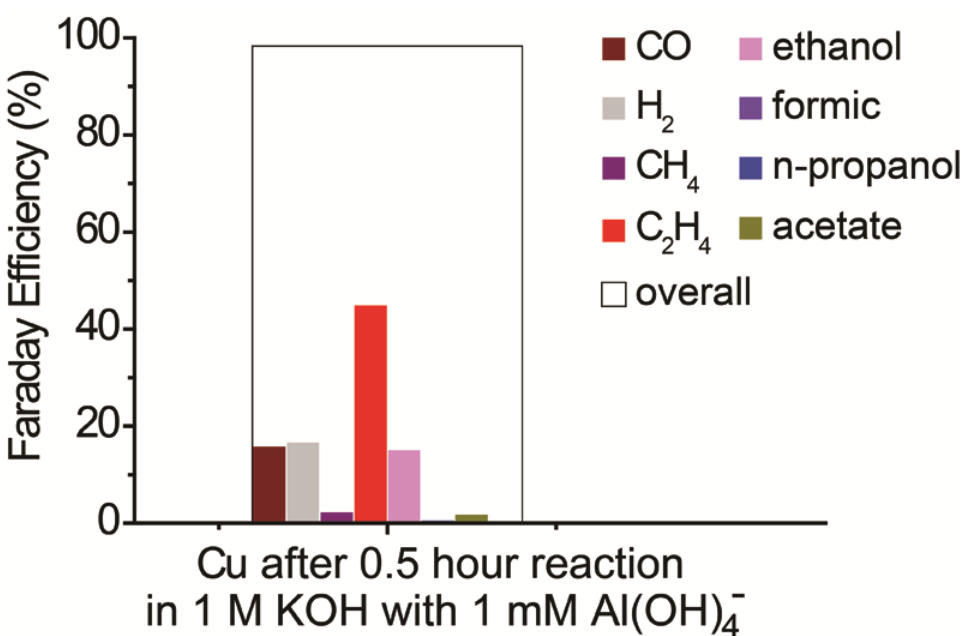
Supplementary Information Figure 15 | EDX analysis of an evaporated-etched Al-on-Cu sample after 5 hours CO₂ electroreduction at 600 mA cm⁻² (-1.8 to -2.0 V_{RHE}) in the 1 M KOH electrolyte. a, EDX mapping. b, EDX spectrum. c, Elemental concentrations. Potassium was observed on the surface after the reaction.



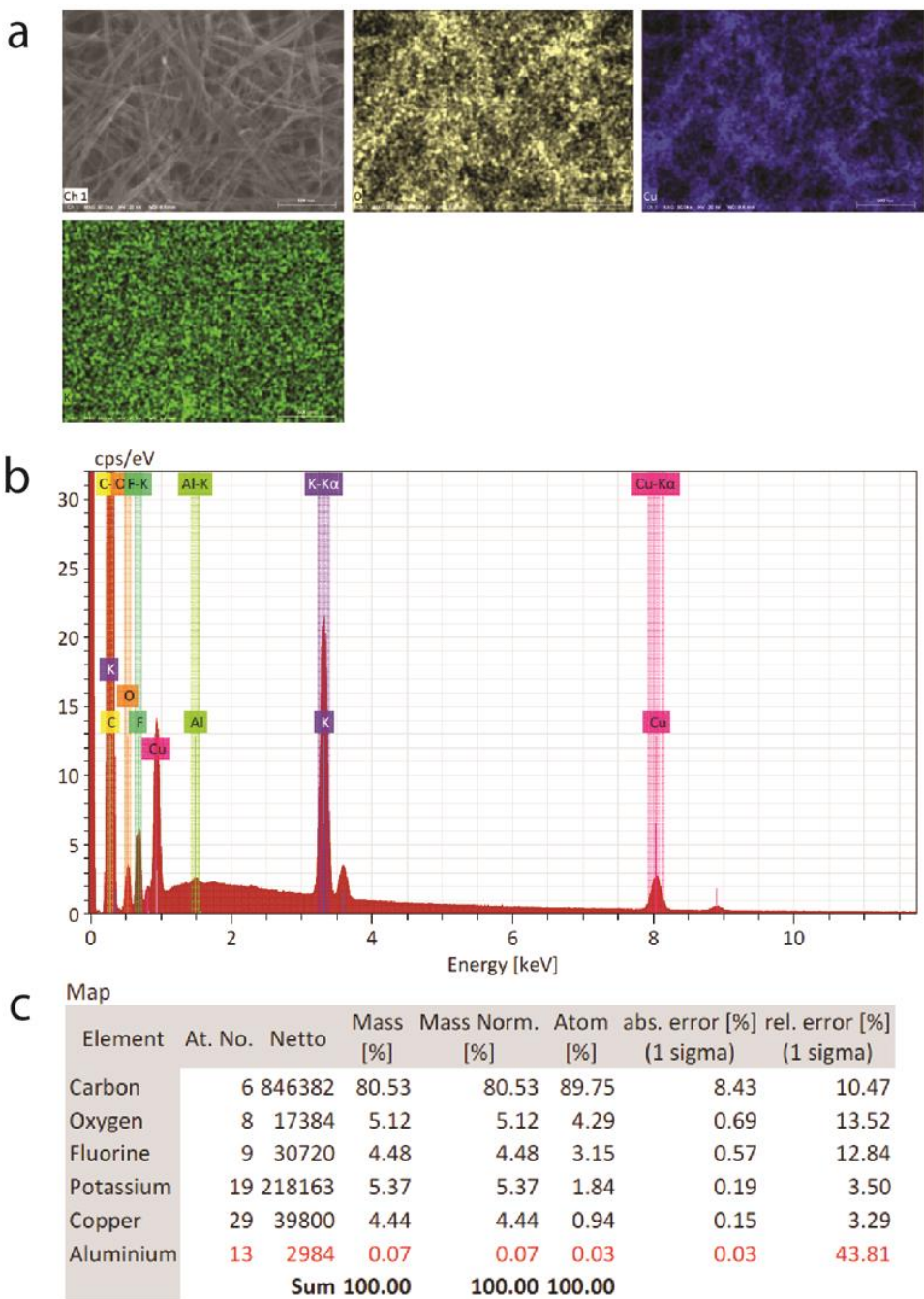
Supplementary Information Figure 16 | EDX analysis of a pure Cu catalyst after half-hour CO₂ electroreduction in 1 M KOH with 1 mM Al(OH)₄⁻. **a**, EDX mapping. **b**, EDX spectrum. **c**, Elemental concentrations. Fluorine was from the PTFE/carbon layer in the gas diffusion electrode. Al was electrodeposited on Cu at an applied current density of 600 mA cm⁻². Therefore, dissolving Al into solution was avoided.



Supplementary Information Figure 17 | Auger electron spectroscopic analysis of a pure Cu catalyst after 0.5-hour CO₂ electroreduction at 600 mA cm⁻² in 1 M KOH with 1 mM Al(OH)⁻. **a**, Auger secondary electron microscopic image. **b**, Auger spectroscopic survey and narrow-scan spectra. **c**, Concentrations of Cu and Al.

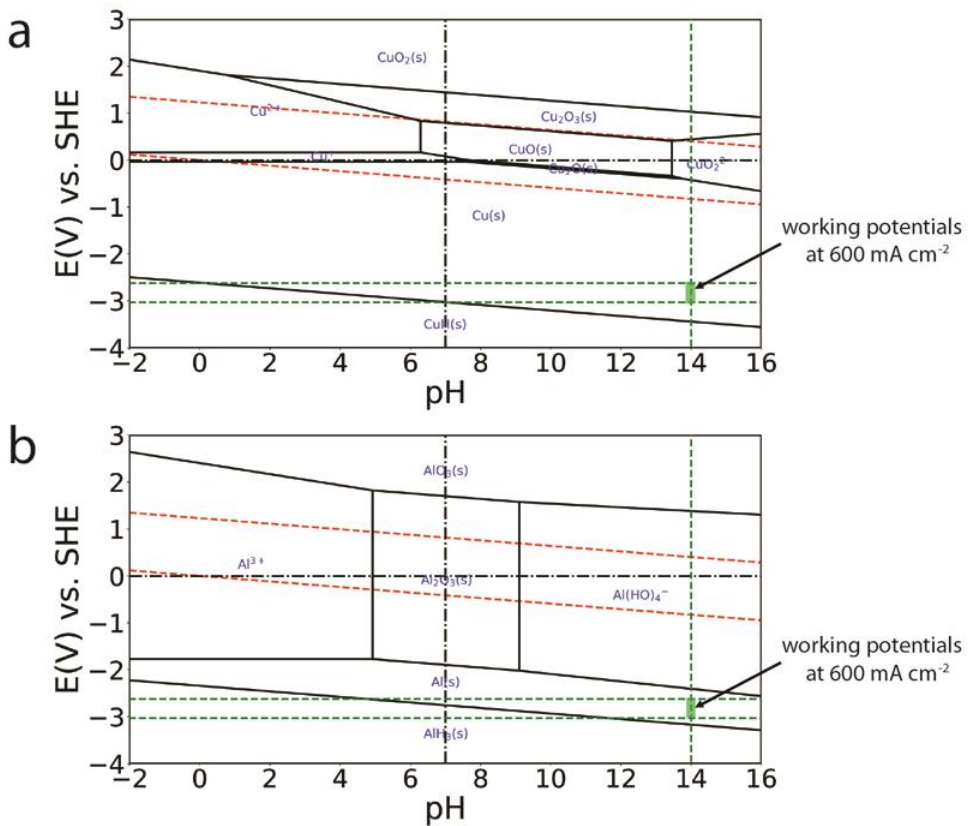


Supplementary Information Figure 18 | CO₂ electroreduction performance. Faradaic efficiencies for gaseous products with a pure Cu catalyst at a constant current density of 600 mA cm⁻² in 1 M KOH with the presence of 1 mM Al(OH)₄⁻ obtained from Chronopotentiometry tests.



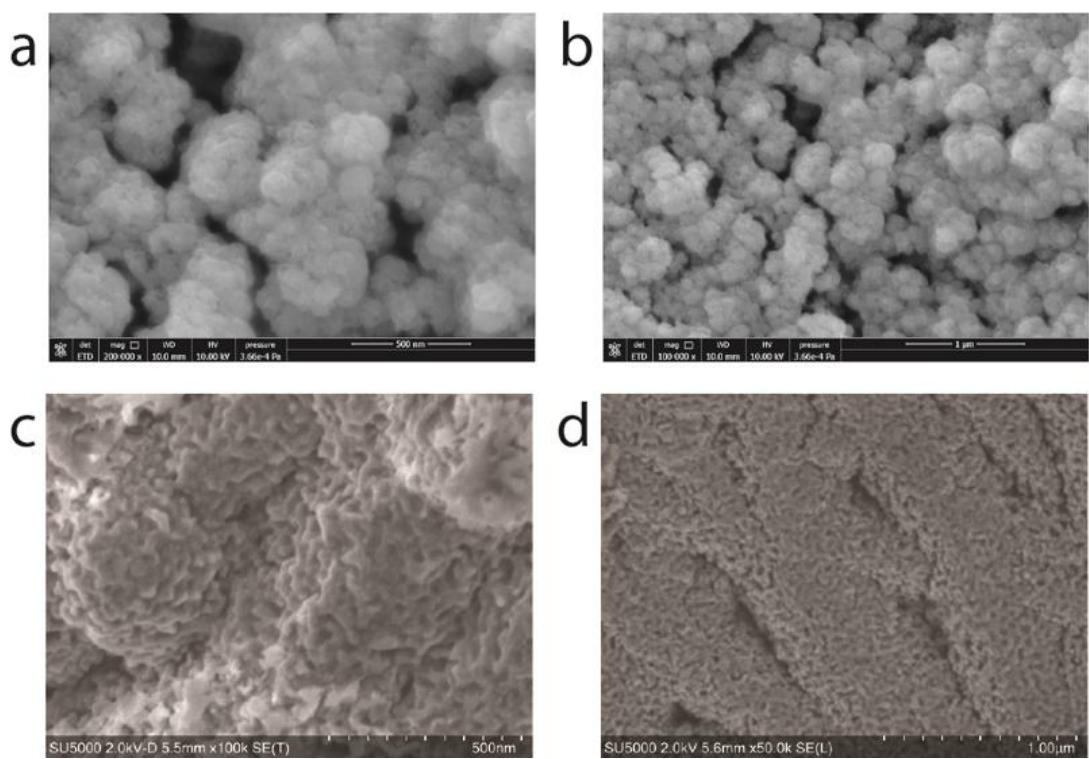
Supplementary Information Figure 19 | EDX analysis of a pure Cu after immersing in 1 M KOH with 1 mM Al(OH)₄⁻ for 0.5 hour. a, EDX mapping. b, EDX spectrum. c, Elemental concentrations. We manually selected Al which was automatically marked in red by EDX software (Esprit 2.1) with a large error of 43.81%, indicating Al was actually out of the EDX detection limit. In SEM image in Supplementary Information Figure 14a, the morphology was also changed. Most of Cu dissolved into 1 M KOH leaving thin Cu(OH)₂ nanowires to be

dissolved.

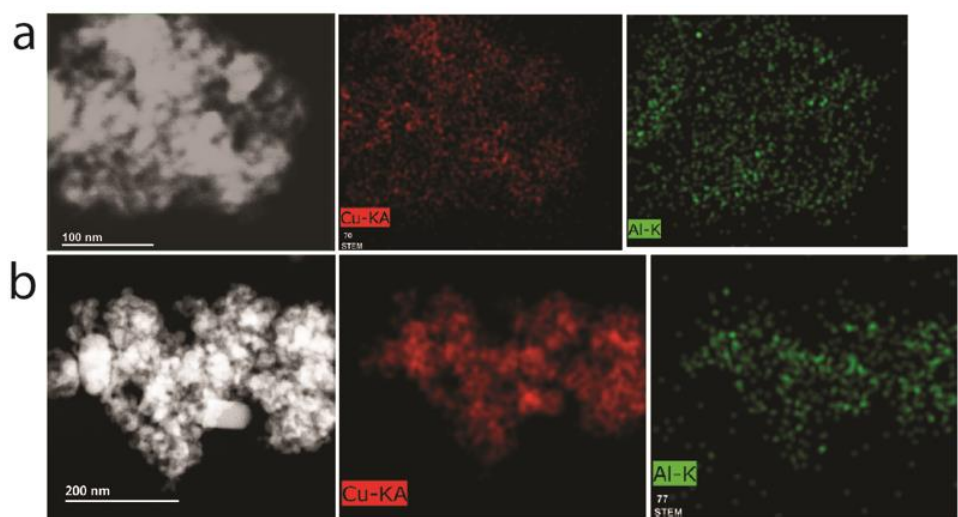


Supplementary Information Figure 20 | Pourbaix diagrams. Pourbaix diagrams of **a**, Cu and **b**, Al at ionic concentrations of 1 μM . The potentials versus the standard hydrogen electrode (V vs. SHE) can be converted to the reversible hydrogen electrode scale (V vs. RHE) according to the Nernst equation, $V \text{ vs. RHE} = V \text{ vs. SHE} + 0.059 \times \text{pH}$.

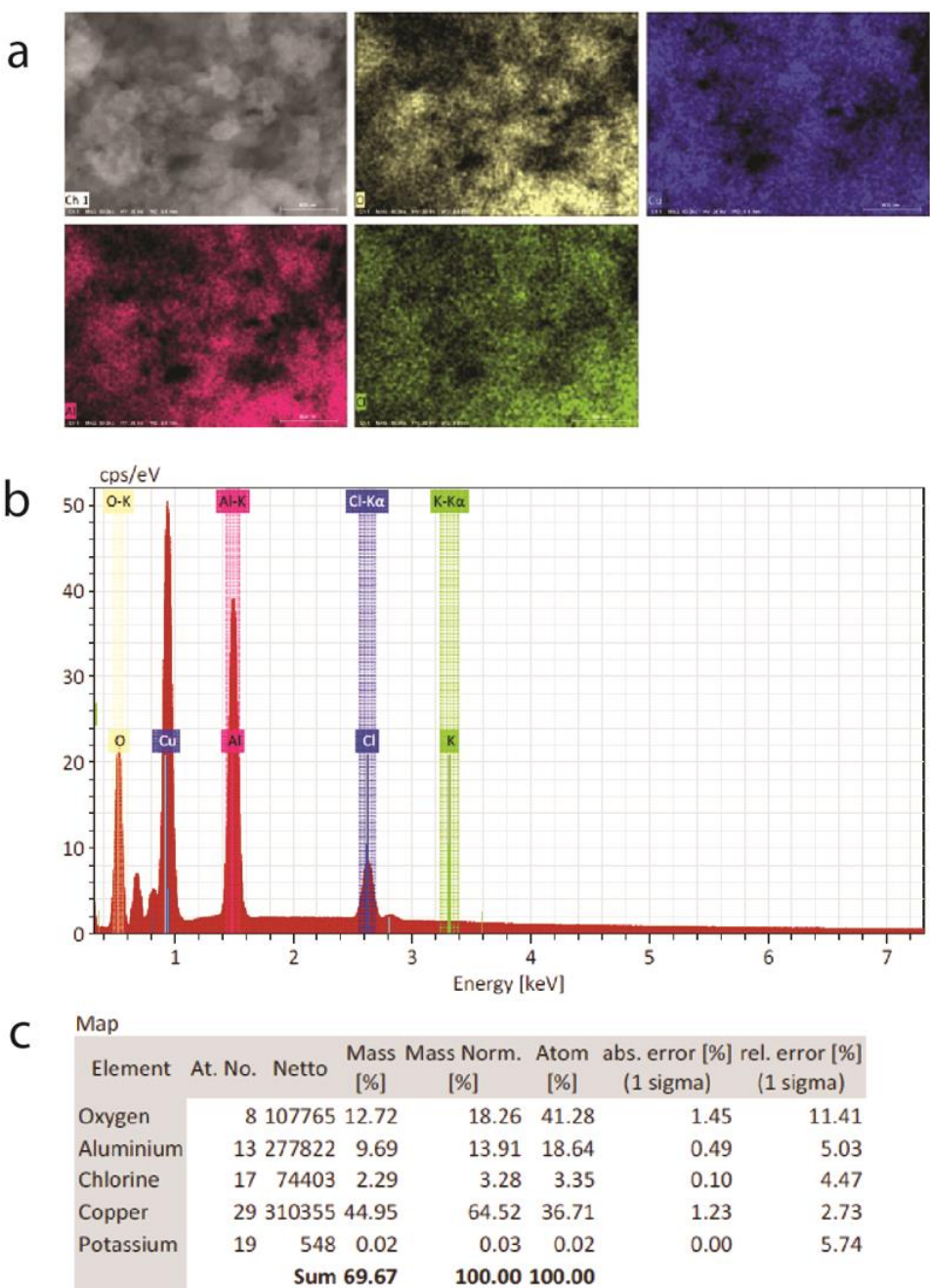
According to the Pourbaix diagrams, Cu metal is cathodically protected at potentials more negative than ca. -0.4 V_{SHE} which corresponds to ca. 0.43 V_{RHE} at pH 14 (1 M KOH) and ca. 0.48 V_{RHE} at pH 15 (10 M KOH). Al metal is cathodically protected at potentials more negative than -2.3 V_{SHE}, which corresponds to -1.47 V_{RHE} at pH 14 and -1.41 V_{RHE} at pH 15.



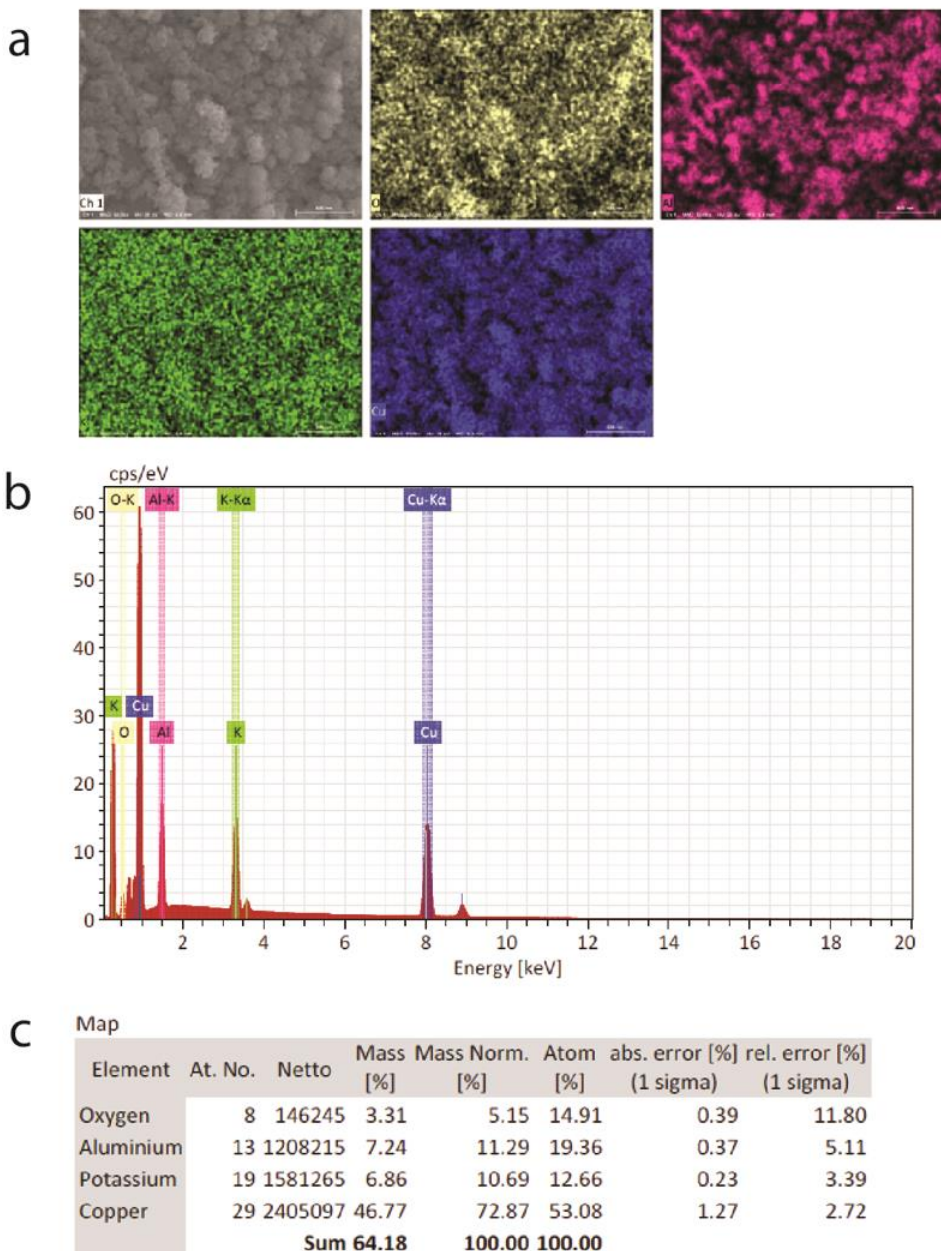
Supplementary Information Figure 21 | Top-view SEM images of the de-alloyed Cu-Al. a-b, De-alloyed Cu-Al catalyst prepared on a C-GDL substrate by physical evaporation and chemical etching. **c-d,** De-alloyed Cu-Al catalyst prepared on a PTFE substrate by co-sputtering and chemical etching.



Supplementary Information Figure 22 | EDX analyses in TEM of de-alloyed Cu-Al catalysts. **a**, as-prepared de-alloyed Cu-Al catalyst. **b**, de-alloyed Cu-Al catalyst after 5 hours CO₂ electroreduction in 1 M KOH at 600 mA cm⁻² in a flow-cell configuration.

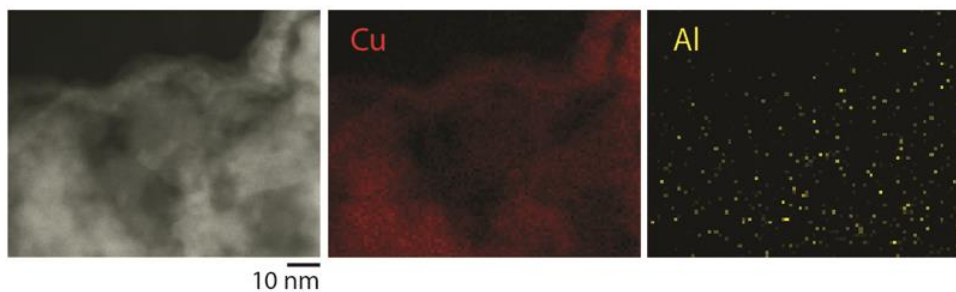


Supplementary Information Figure 23 | EDX analysis in SEM of the as-prepared de-alloyed Cu-Al catalyst before CO₂ electroreduction. a, EDX mapping. b, EDX spectrum. c, Elemental concentrations. Chlorine was detected because of the use of a 5 wt% HCl solution in the etching process to prepare a de-alloyed Cu-Al catalyst.

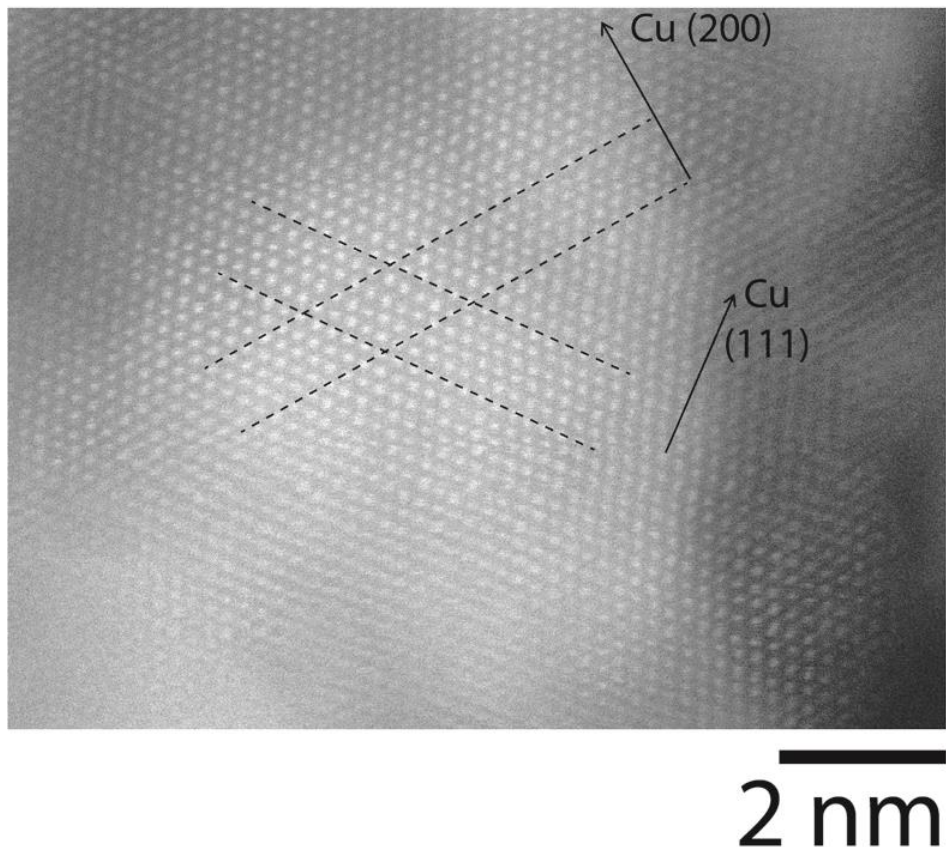


Supplementary Information Figure 24 | EDX analysis in SEM of a de-alloyed Cu-Al catalyst after 5 hours CO₂ electroreduction at 600 mA cm⁻² (-1.8 to -2.0 V_{RHE}) in 1 M KOH.

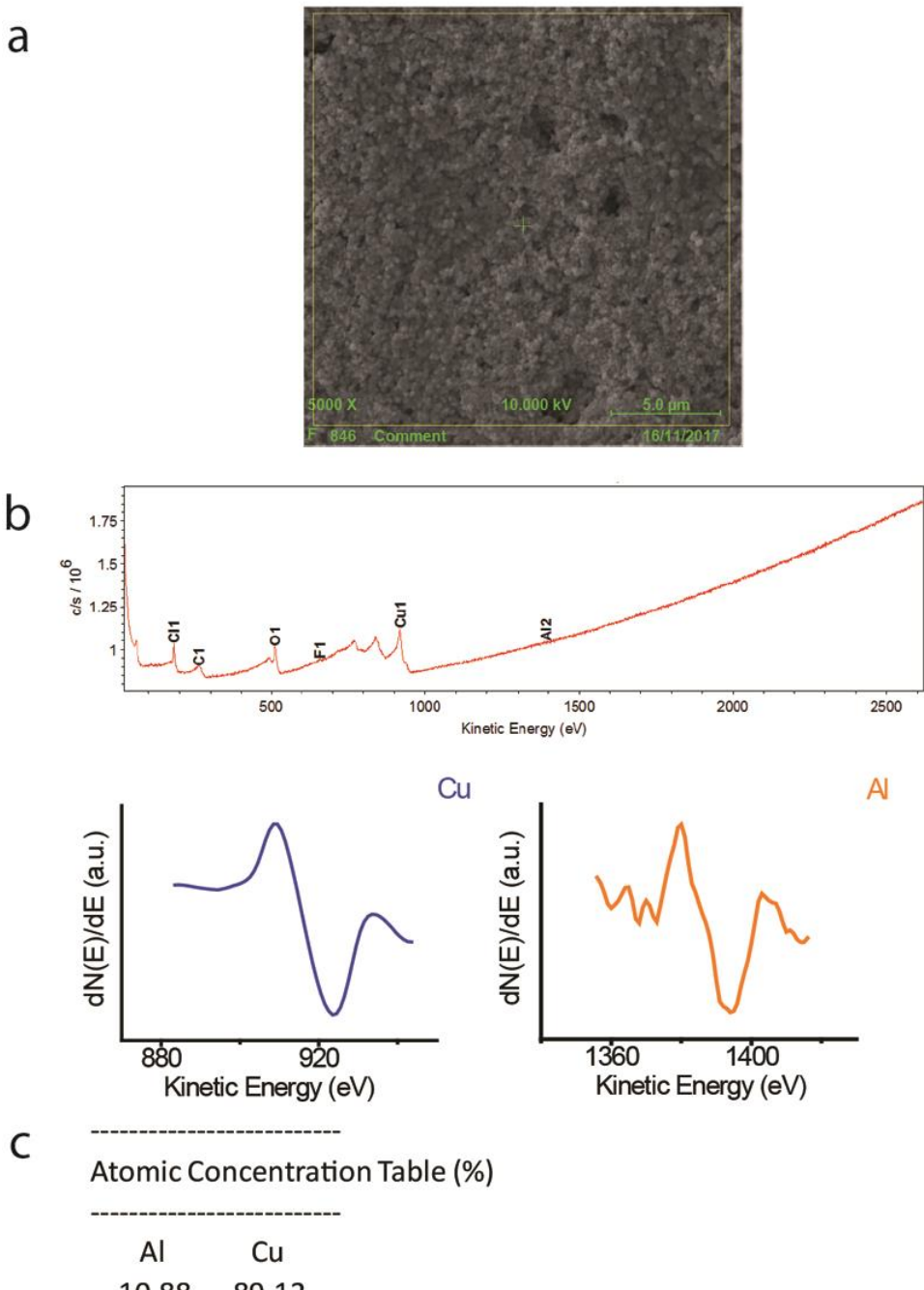
a, EDX mapping. **b**, EDX spectrum. **c**, Elemental concentrations. Potassium was detected because of the use of KOH electrolyte in CO₂ electroreduction.



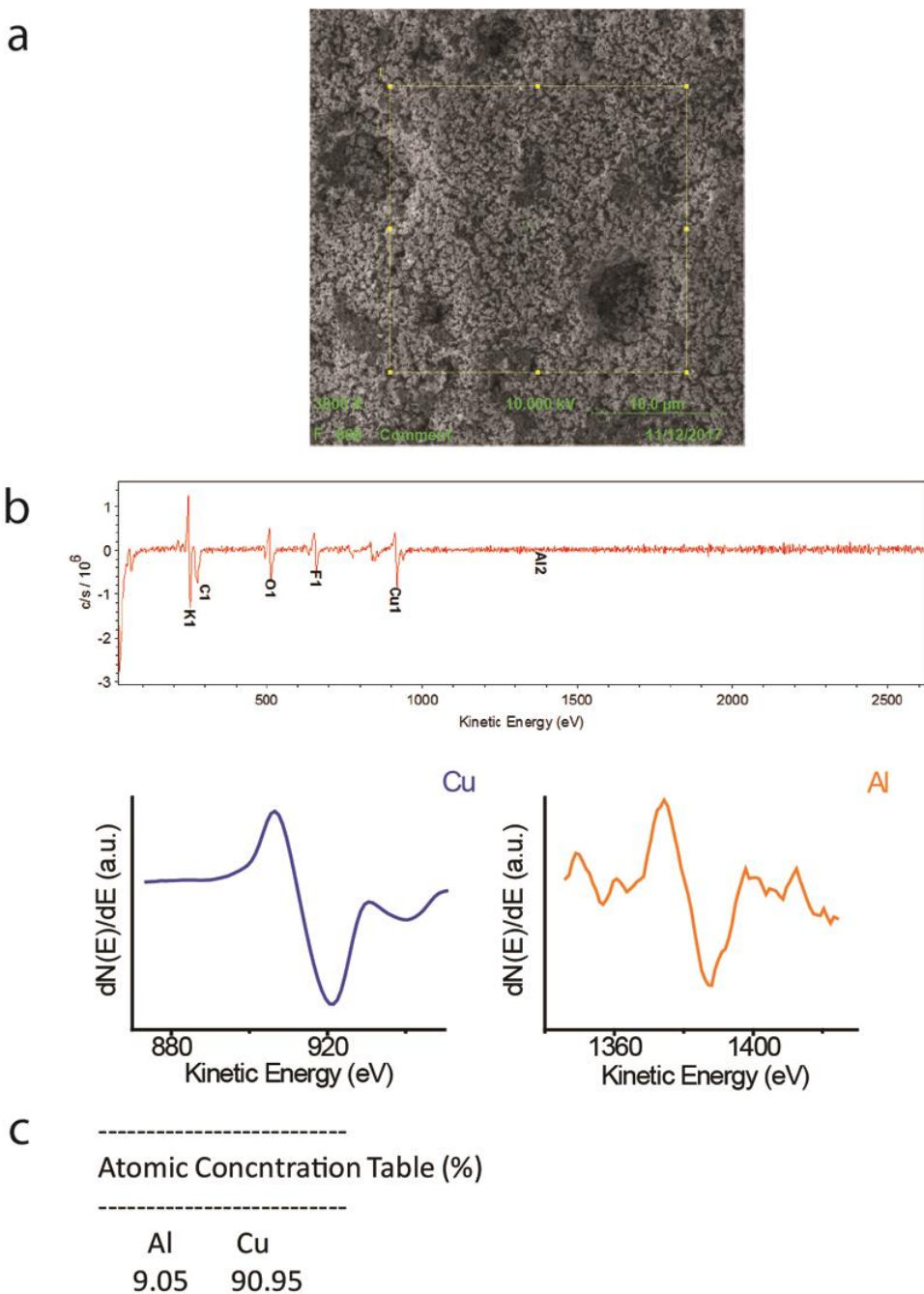
Supplementary Information Figure 25 | HAADF-STEM with EELS mapping images of Cu and Al of a de-alloyed Cu-Al catalyst after 5 hours CO₂ electroreduction. A nanoporous structure was observed with the de-alloyed Cu-Al after the CO₂ electroreduction.



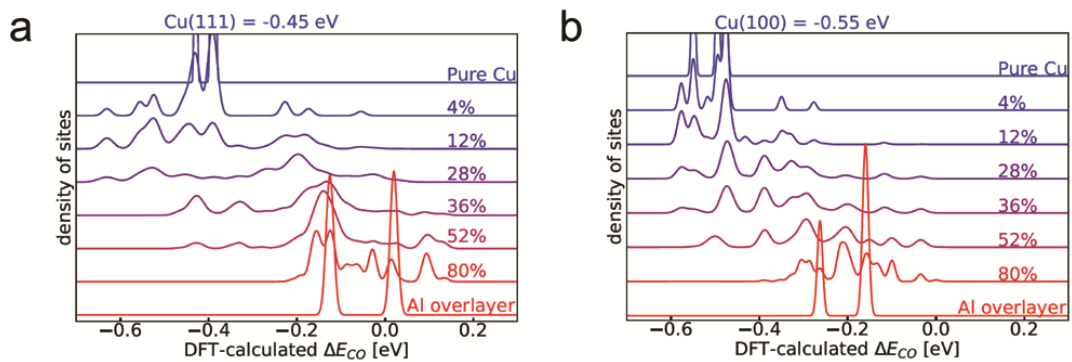
Supplementary Information Figure 26 | STEM-ADF image of the de-alloyed Cu-Al catalyst. The observation was performed in the same area where we performed EELS analysis (Fig. 2c).



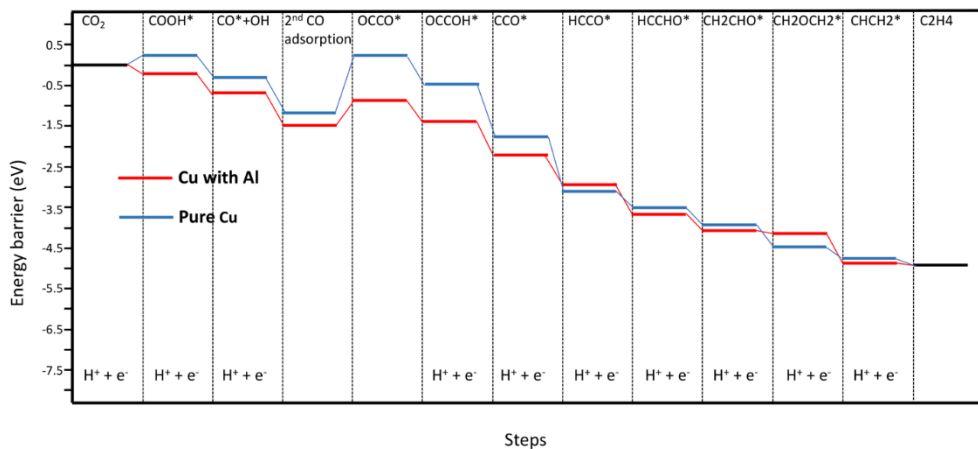
Supplementary Information Figure 27 | Auger electron spectroscopic analysis of an as-prepared de-alloyed Cu-Al catalyst. **a**, Auger secondary electron microscopic image. **b**, Auger spectroscopic survey and narrow-scan spectra. **c**, Concentrations of Cu and Al.



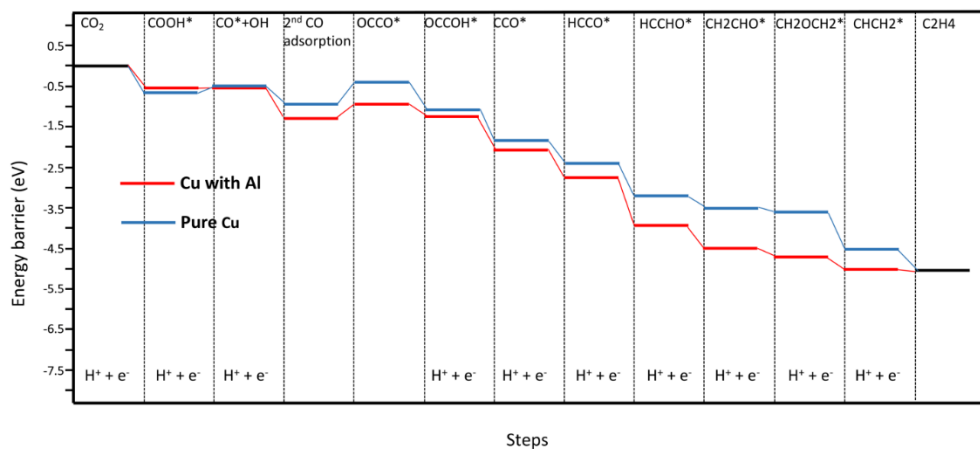
Supplementary Information Figure 28 | Auger electron spectroscopic analysis of a de-alloyed Cu-Al catalyst after 5 hours CO₂ electroreduction at 600 mA cm⁻² in 1 M KOH. **a**, Auger secondary electron microscopic image. **b**, Auger spectroscopic survey and narrow-scan spectra. **c**, Concentrations of Cu and Al.



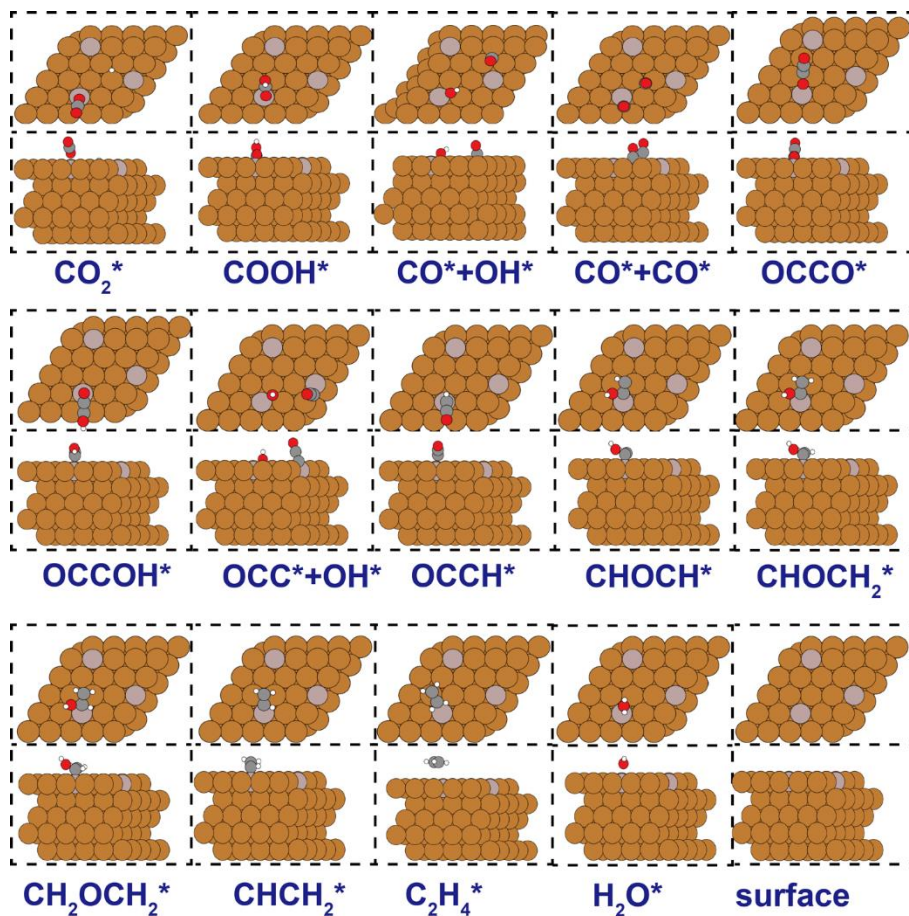
Supplementary Information Figure 29 | ML and DFT analyses of the (111) and (100) facets across varying ratios of Al concentrations. **a, b,** The distribution of ΔE_{CO} values for the adsorption sites on Cu (111) and (100) surfaces with different amounts of Al replacement on the top layer of atoms.



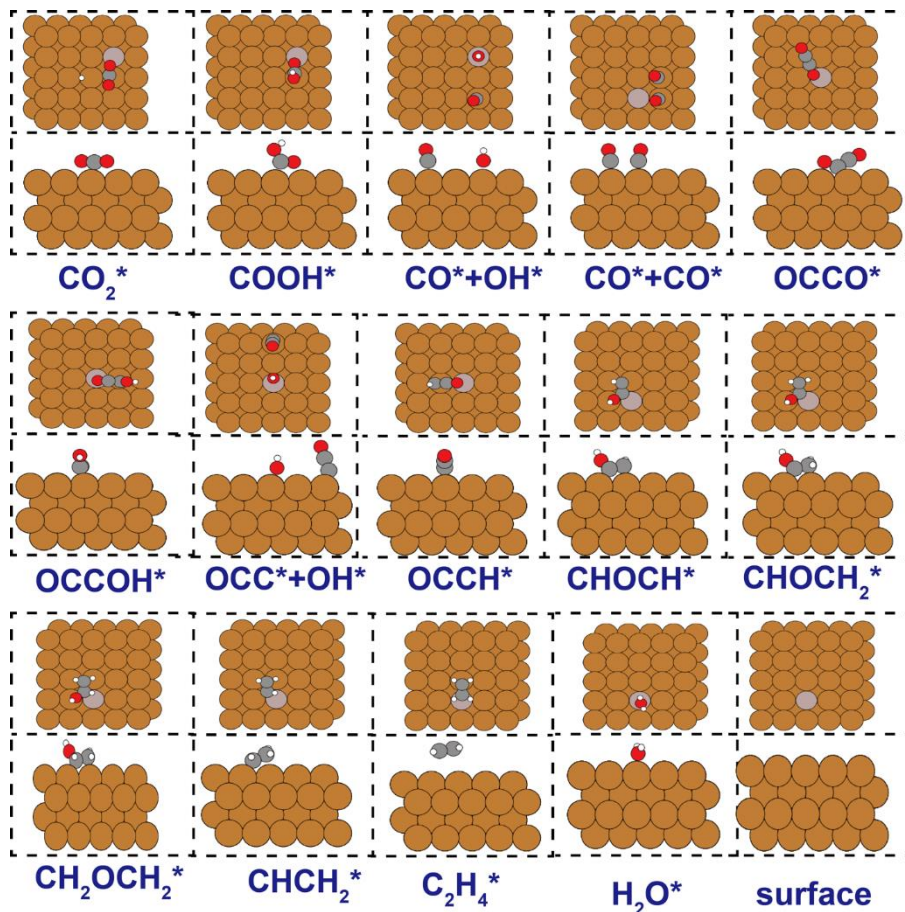
Supplementary Information Figure 30 | Reaction Gibbs free energy diagram. Reaction Gibbs free energy diagram from adsorbed CO_2 to C_2H_4 on the pure Cu (100) surface (blue line) and 12% Al incorporated Cu (111) surface (red line) with -0.5V applied potential.



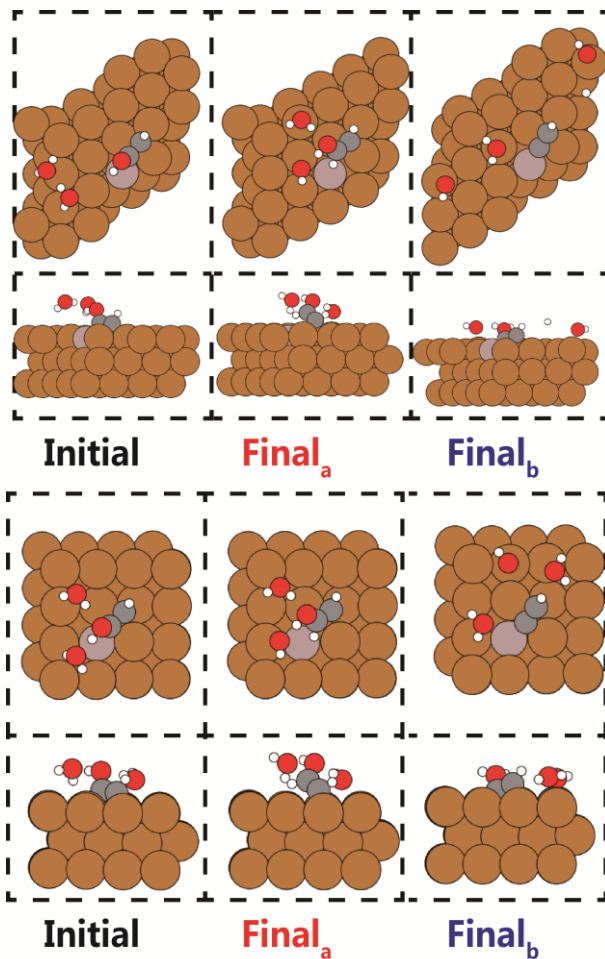
Supplementary Information Figure 31 | Reaction Gibbs free energy diagram. Reaction Gibbs free energy diagram from adsorbed CO_2 to C_2H_4 on the pure Cu (100) surface (blue line) and 4% Al incorporated Cu (100) surface (red line) with -0.5V applied potential.



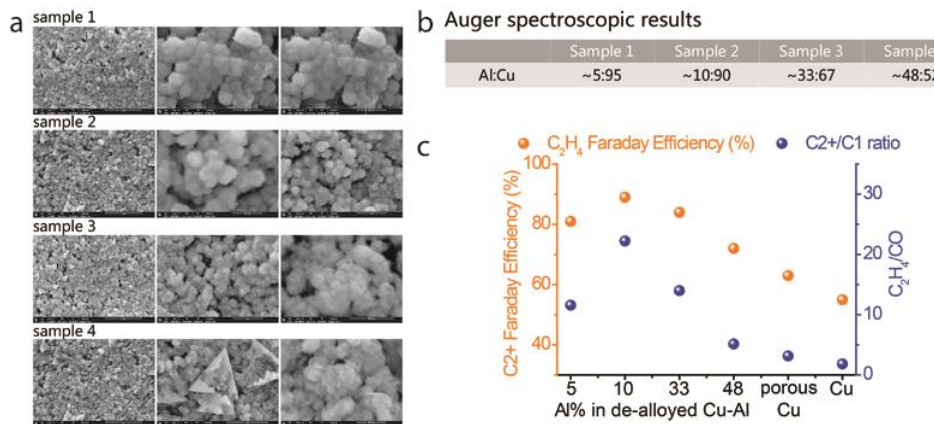
Supplementary Information Figure 32 | A possible pathway with intermediates in the CO₂ electroreduction. Optimized geometries of CO₂ reduction intermediates on the 12% Al incorporated Cu (111) surface.



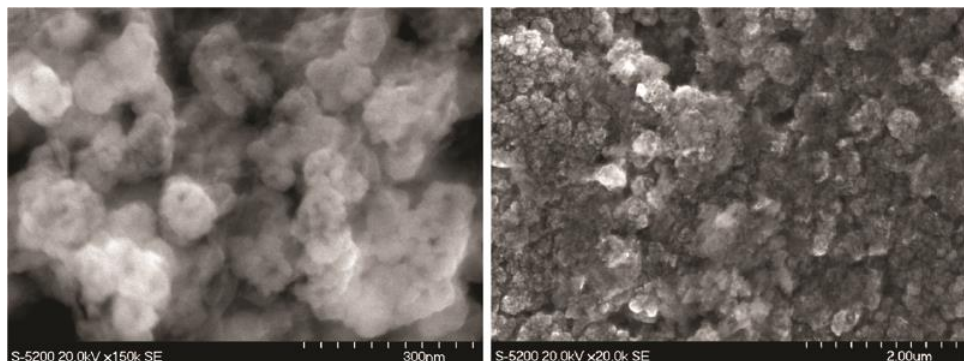
Supplementary Information Figure 33 | A possible pathway with intermediates in the CO₂ electroreduction. Optimized geometries of CO₂ reduction intermediates on the 4% Al incorporated Cu (100) surface.



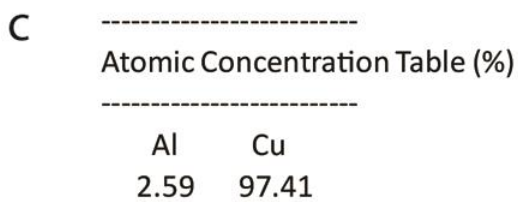
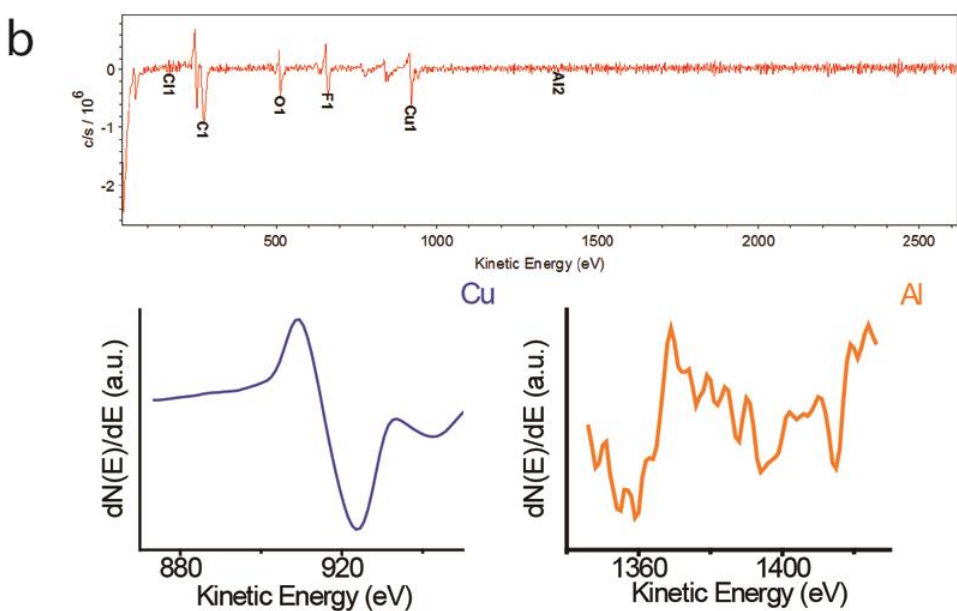
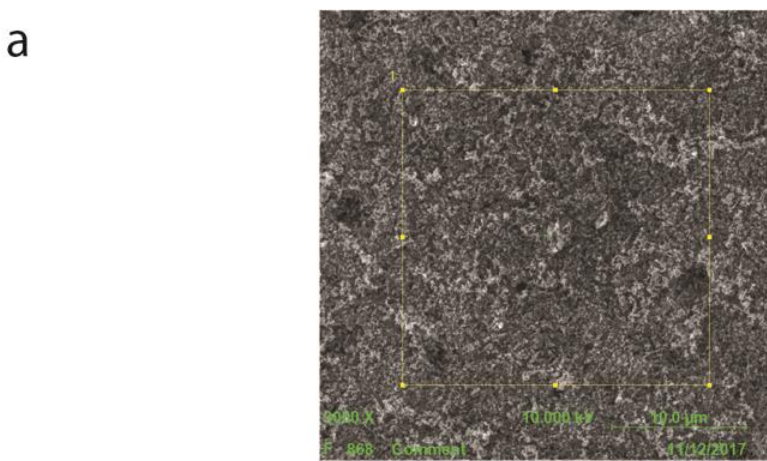
Supplementary Information Figure 34 | Initial and final intermediates of forming ethanol (red) and C₂H₄ (blue) on the 12% Al incorporated Cu (111) and 4% Al incorporated (100) surfaces. A possible pathway with intermediates in the CO₂ electroreduction. According to the previous work reported by Goddard *et al.*^{S26}, surface water may play an important role to determine the key intermediates that branch toward ethanol and C₂H₄ production especially at high pH conditions. We use their method to calculate the reaction energy of the key intermediates on the 12% incorporated Cu (111) and 4% Al incorporated Cu (100) surfaces. The reaction energy for forming ethanol are 0.343 eV and 0.223 eV larger than that for forming C₂H₄ on the Al incorporated Cu (111) and Cu (100) surfaces, respectively.



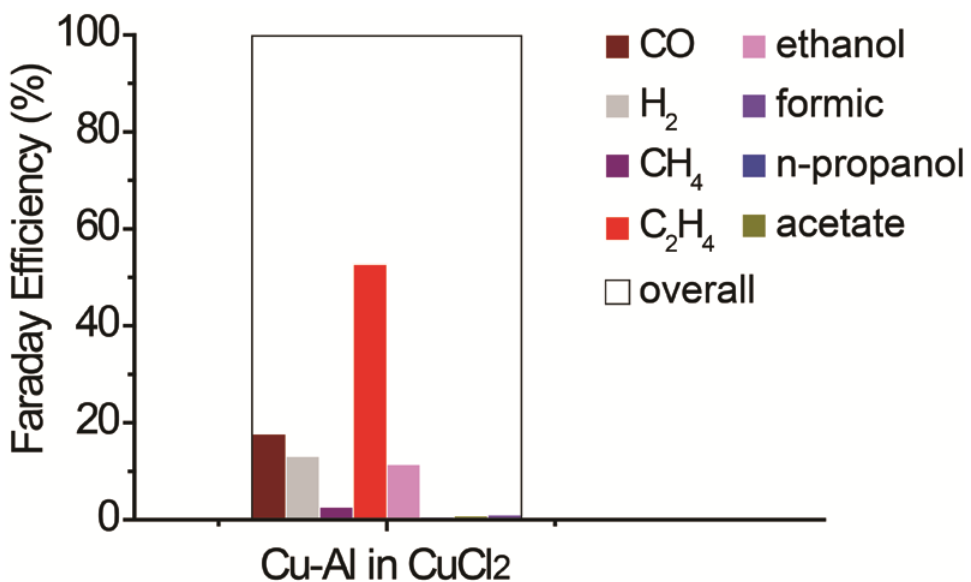
Supplementary Information Figure 35 | De-alloyed Cu-Al with different surface Al concentrations. **a**, SEM images of de-alloyed Cu-Al with different etching time. **b**, Al concentrations on surfaces determined by surface-sensitive Auger spectroscopic analysis. Surface Al concentrations roughly varied from 4-48% by controlling the etching time. **c**, Faradaic efficiencies of C₂₊ and C₂₊/C₁ ration with de-alloyed catalysts at different surface Al concentrations.



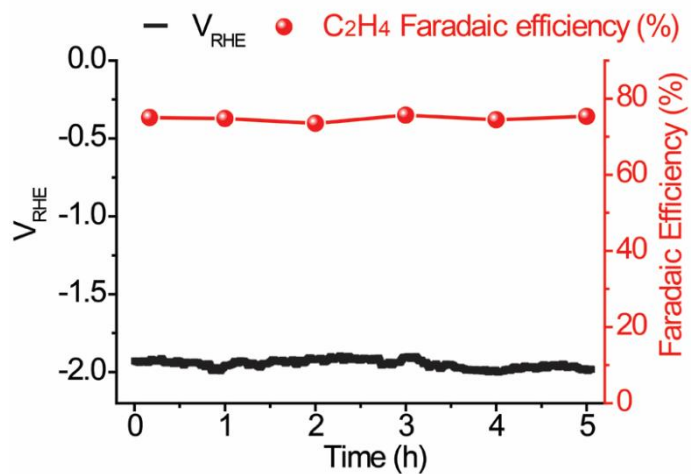
Supplementary Information Figure 36 | SEM images of a de-alloyed Cu-Al catalyst soaked in 10 mM CuCl₂ for 10 minutes. 10 minutes is an optimal time for use to roughly maintain catalyst nanoporosity while replacing surface Cu with Al by the displacement reaction of 2Al + 3CuCl₂ → 2AlCl₃ + 3Cu. With a prolonged displacement reaction, nanopores were gradually blocked by the precipitated Cu.



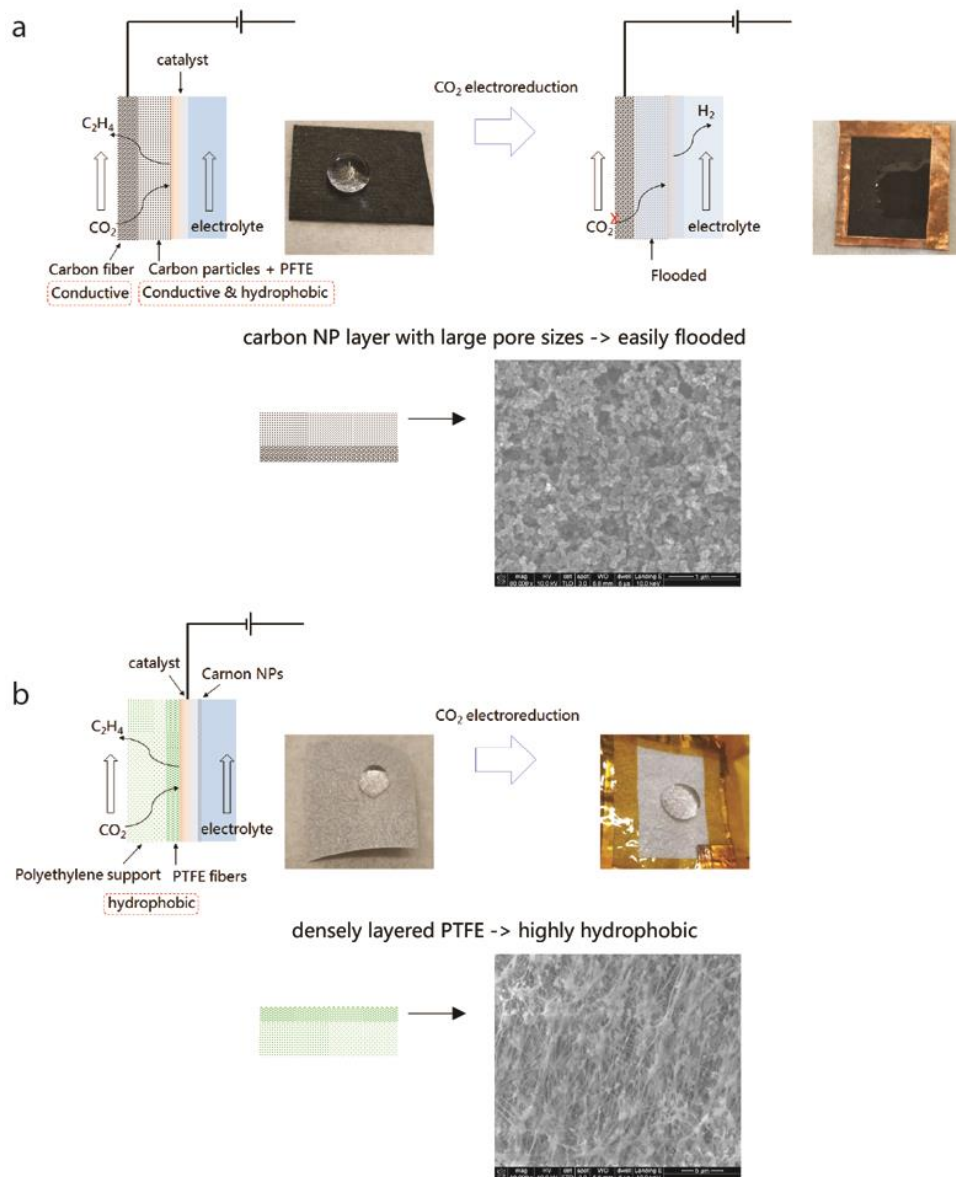
Supplementary Information Figure 37 | Auger electron spectroscopic analysis of a de-alloyed Cu-Al catalyst soaked in 10 mM CuCl₂ solution for 0.5 hour. a, Auger secondary electron microscopic image. b, Auger spectroscopic survey and narrow-scan spectra. c, Concentrations of Cu and Al. The Al concentration calculated from Al narrow-scan spectrum is already close to the AES detecting limit.



Supplementary Information Figure 38 | CO₂ electroreduction performance. Faradaic efficiencies for all products at an applied current density of 600 mA cm⁻² obtained with of a de-alloyed Cu-Al catalyst after soaking in 10 mM CuCl₂ solution for 10 minutes.



Supplementary Information Figure 39 | CO₂ electroreduction stability of the de-alloyed Cu-Al/C-GDL electrode. The CO₂ electroreduction activity of a de-alloyed Cu-Al/C-GDL electrode at an applied current density of 600 mA cm⁻². Left axis: potential (V vs. RHE) vs. time (s), right axis: C₂H₄ Faradaic efficiency (%) vs. time (s).



Supplementary Information Figure 40 | Configuration of de-alloyed Cu-Al catalysts on (a)

C-GDL and (b) PTFE substrates for CO_2 electrolysis in a flow cell system. Optical images

were taken on the backside of the samples to show the hydrophobicity of **a**, Cu-Al/C-GDL

before and after 5 hours stability test in 1 M KOH, and **b**, Cu-Al/PTFE before and after 50

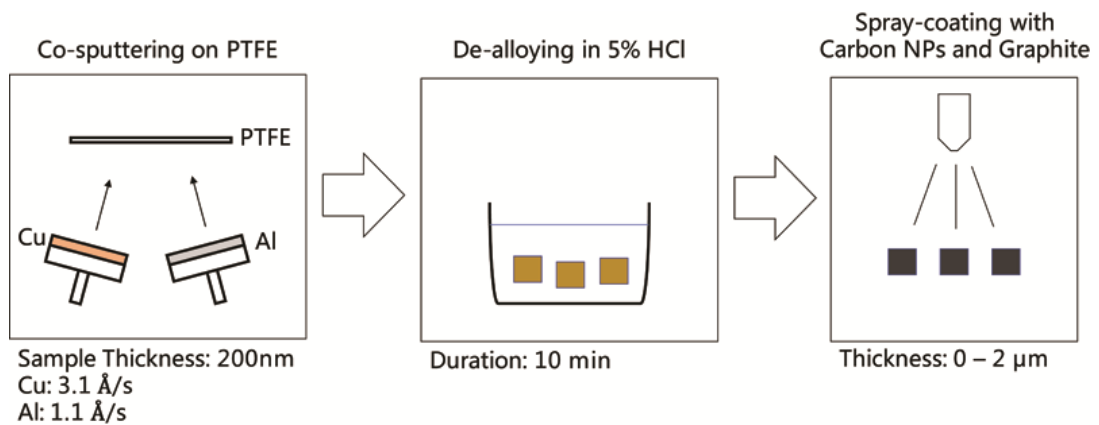
hours stability test in 3 M KOH with 3M KI solutions.

The difference between GDL and PTFE:

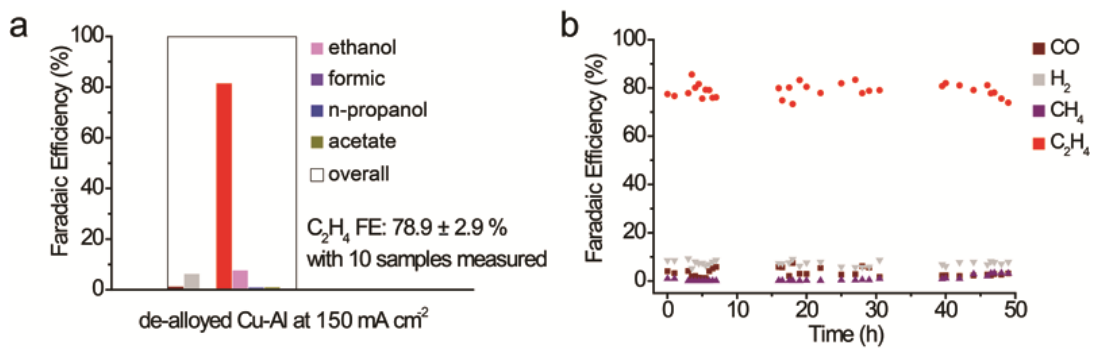
- The porous GDL is made of carbon nanoparticles (for conductivity) coated with a small amount of PTFE on the surface (for hydrophobicity). Large porosity ensures sufficient CO_2

diffusion so that we obtain a higher CO₂-reduction current density (j-v curve in Figure 3a in the manuscript). However, it can't provide enough surface tension to hold the liquid above so that GDL is easily flooded and thus it gradually losses stability during the reaction.

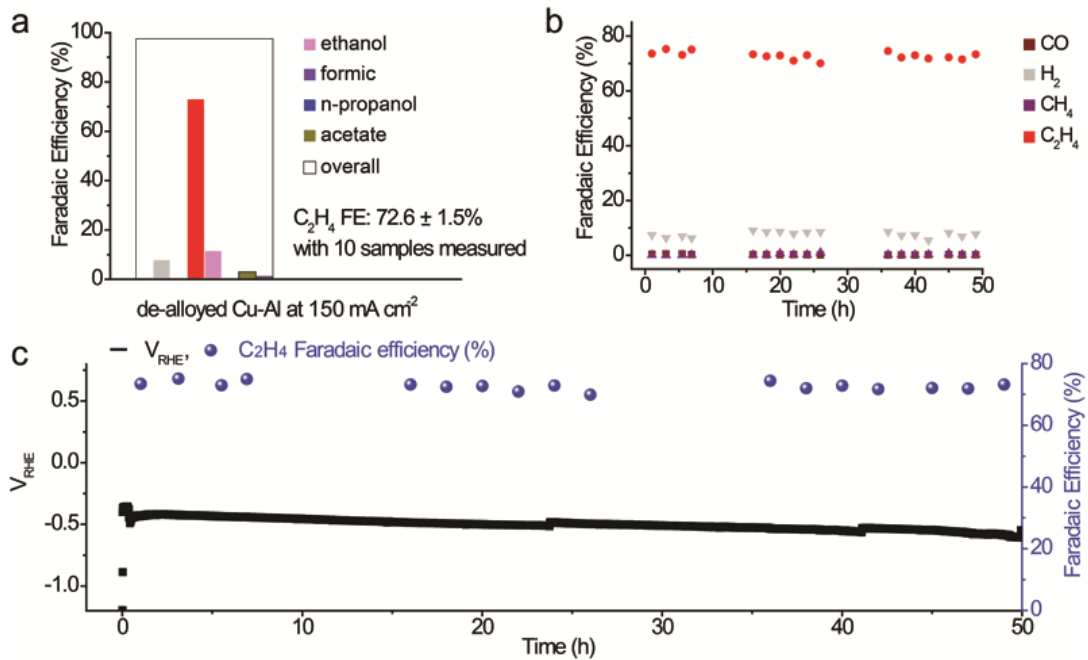
- The densely layered PTFE offers strong hydrophobicity to keep the liquid/gas/solid interface for long-term electrolysis operation, but CO₂ diffusion is limited due to its reduced porosity so that the CO₂-reduction current density is lower (Figure 4a in the manuscript).



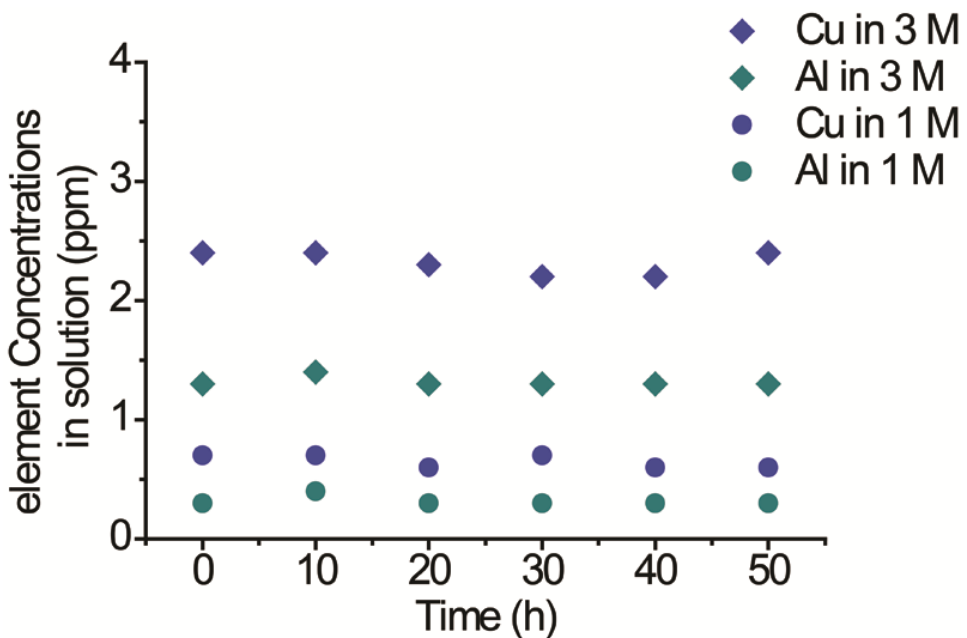
Supplementary Information Figure 41 | Co-sputtering, chemical etching and spray coating to make graphit/carbon NPs/de-alloyed Cu-Al /PTFE substrates.



Supplementary Information Figure 42 | CO₂ electroreduction performance with graphite/carbon NPs/de-alloyed Cu-Al/PTFE samples in a 1 M KOH electrolyte. **a**, Faradaic efficiencies for all products at an applied current density of 400 mA cm⁻² with 10 distinct samples measured. **b**, Faradaic efficiency of gas products vs. time during the stability test.



Supplementary Information Figure 43 | CO₂ electroreduction performance with graphite/carbon NPs/de-alloyed Cu-Al/PTFE samples in a 3 M KOH and 3 M KI electrolyte. **a**, Faradaic efficiencies for all products at an applied current density of 150 mA cm⁻² with 10 distinct samples measured. **b**, Faradaic efficiency of gas products vs. time during the stability test. **c**, The CO₂ electroreduction stability at an applied current density of 150 mA cm⁻². Left axis: potential (V vs. RHE) vs. time (s), right axis: C₂H₄ Faradaic efficiency (%) vs. time (s). Note that we passed a small amount of 1 M KI catholyte (pH 5.5-6.5) as a buffer electrolyte before passing the real testing KOH catholyte to protect Cu-Al catalyst from possible dissolution into KOH catholyte at the time when there is no working potential applied. The small amount of KI was then pumped out of the flow-cell system after use as a buffer electrolyte at the beginning stage of the test. We convert the potential to V_{RHE} using the equation: V_{RHE} = V_{Ag/AgCl} + 0.199 + 0.059 × pH, in which we use the testing KOH pH values for calculation. The real potentials at time 0 in **c** should be ca. -0.5 V more cathodic.



Supplementary Information Figure 44 | ICP analysis. ICP-AES results of Cu and Al ions in the testing solution with different the testing time. The de-alloyed Cu-Al catalysts on PTFE was measured at 400 mA cm^{-2} in 1 M KOH solution and at 150 mA cm^{-2} in 3 M KOH and 3 M KI solution for 50 hours.

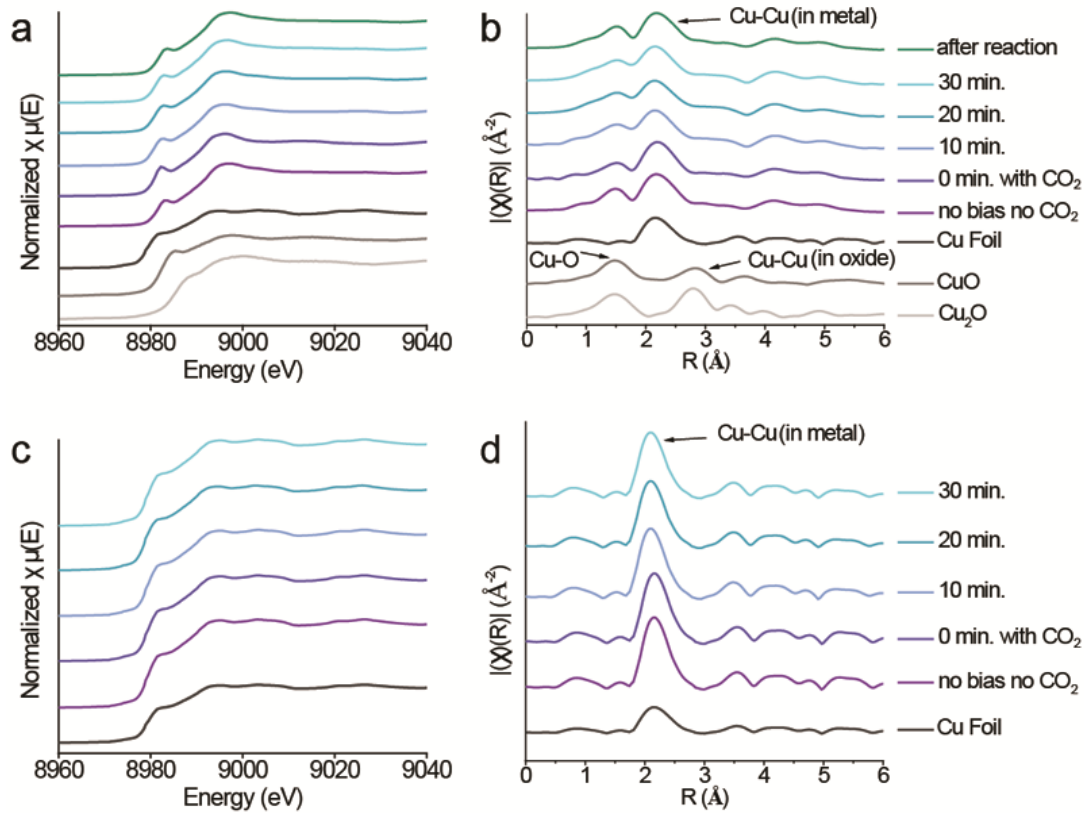
As shown in the Supplementary Information Fig. 44, the concentrations of Cu and Al at time 0 are the Cu and Al impurity concentrations in KOH catholyte without performing CO_2 electroreduction, thus there is no obvious leaching of Cu and Al into the electrolyte.

We further conduct the CO_2 electroreduction by using a large amount of catholyte (10 liter 1 M KOH, 10 kg, and 10 liter 3 M KOH + 3 M KI, 10 kg) for a very small amount of Cu-Al catalyst (1 cm^2 area and 200 nm thick Cu-Al layer). We used ICP-AES to confirm that 1 cm^2 and 200 nm thick Cu-Al sample contained $\sim 80 \mu\text{g}$ Cu and $\sim 30 \mu\text{g}$ Al, by dissolving a different 1 cm^2 and 200 nm thick Cu-Al sample made in the same sputtering batch, and then performing ICP-AES analysis. If 1% of the detected amounts of Cu and Al in the Supplementary Information Fig. 44 are from the leached Cu and Al, the 1 cm^2 and 200 nm thick Cu-Al sample would all

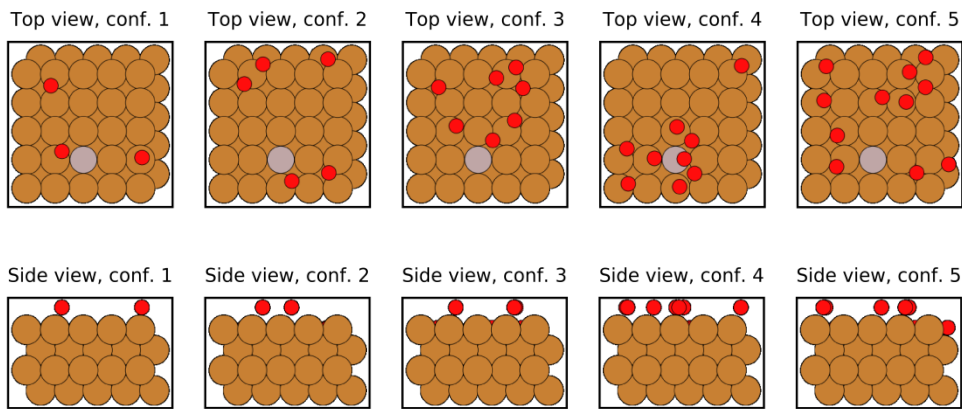
dissolved into the 10 kg catholyte. However, we didn't find any obvious change with the sample after the 50-hour test in both 10 kg 1 M KOH and 3 M KOH + 3 M KI solutions. It means that the assumed dissolved amount of Cu and Al are far below 1% compared to that of impurities in electrolyte. We further dissolved the after-reaction Cu-Al samples into the solution and used ICP-AES to confirm that the weight of Cu and Al is in the same range to that before the reaction.

***In situ* and *ex situ* X-ray absorption studies.**

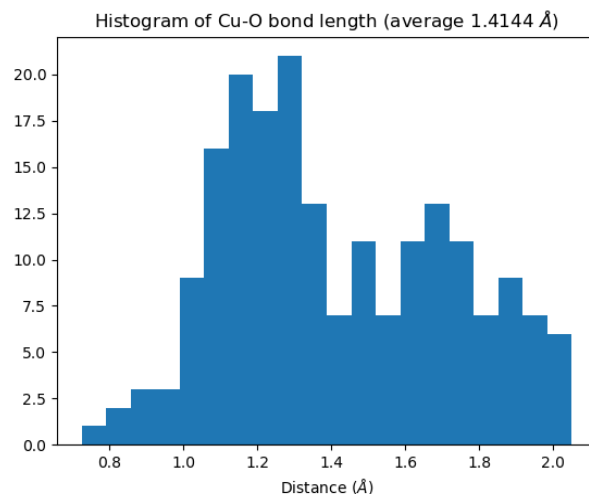
A large amount of Cu-O bonding was visible continuously in the *ex situ* and *in situ* XANES analyses with the de-alloyed Cu-Al catalyst before, during and after the reaction (Supplementary Information Fig. 45). *In situ* Fourier transform extended X-ray absorption fine structure (FT EXAFS) spectra of the de-alloyed Cu-Al catalysts, together with *ex-situ* reference spectra of Cu foil, Cu₂O and CuO, gave precise coordination information. We observed a prominent peak at ~2.2 Å from Cu-Cu contribution, which agrees with the prominent peak of Cu-Cu in Cu foils, and a weak peak at ~1.5 Å, which agrees with the prominent peak of Cu-O in Cu₂O and CuO. As a control, we measured *in situ* XANES with a pure Cu on GDL under the same condition. No obvious oxidation state of Cu was observed (Supplementary Information Fig. 45).



Supplementary Information Figure 45 | *Ex situ* and *in situ* synchrotron analyses of the high-performing de-alloyed Cu-Al catalyst and pure Cu catalyst. a-b, *In situ* X-ray absorption near-edge structure (XANES) spectra of de-alloyed Cu-Al catalyst before, during and after CO₂ electroreduction tests and *ex situ* XANES spectra of Cu foil, Cu₂O, CuO. c-d, *In situ* X-ray absorption near-edge structure (XANES) spectra of pure Cu catalyst before and during CO₂ electroreduction tests and *ex situ* XANES spectra of Cu foil.



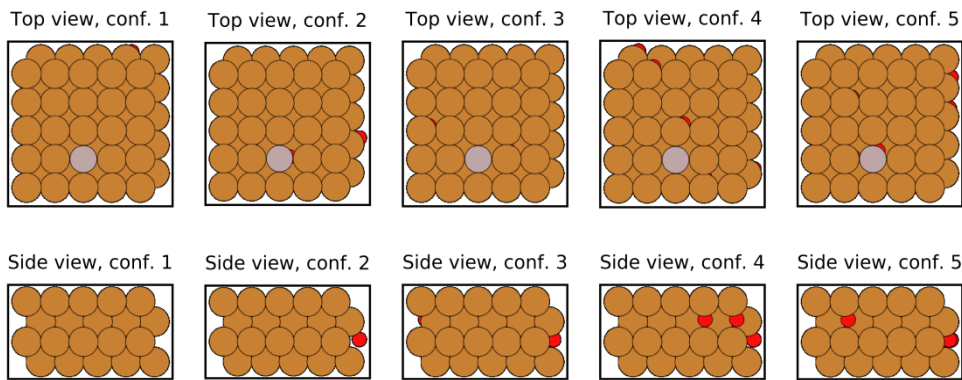
Supplementary Information Figure 46 | Models used to calculate the reaction energies in the rate-determining step of C-C bond making in the CO₂ reduction. 4% Al incorporated Cu (100) surface with different amounts of Cu-O bonds as shown in configurations 1-5.



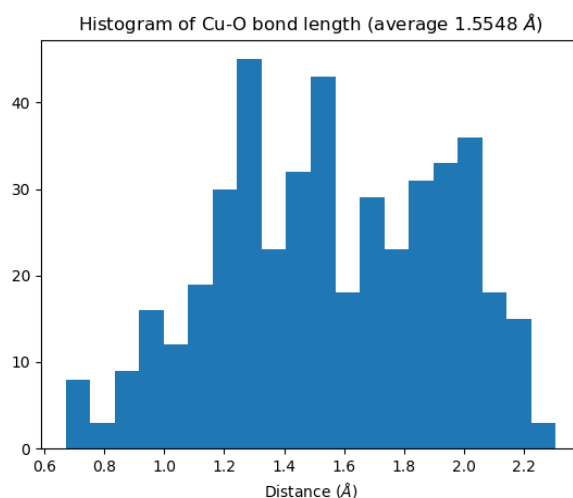
Supplementary Information Figure 47 | The distribution of Cu-O bond length in the Supplementary Information Figure 46.

No.	1	2	3	4	5	Pure Cu
RD step barrier (eV)	0.51	0.52	0.51	0.56	0.53	0.62

Supplementary Information Table S1 | The reaction energies in the rate-determining step of C-C bond making on different configurations in the Supplementary Information Figure 47.



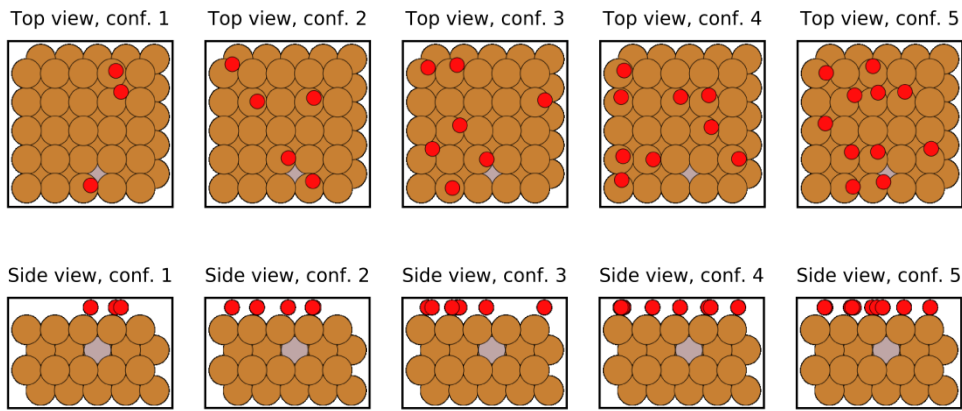
Supplementary Information Figure 48 | Models used to calculate the reaction energies in the rate-determining step of C-C bond making in the CO₂ reduction. 4% Al incorporated Cu (100) surface with different amounts of Cu-O bonds as shown in configurations 1-5.



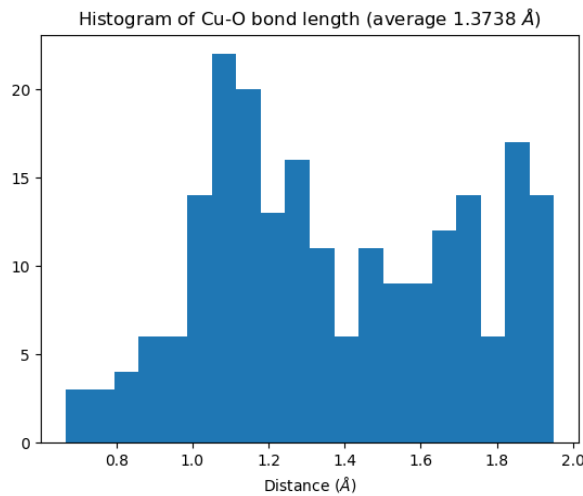
Supplementary Information Figure 49 | The distribution of Cu-O bond length in the Supplementary Information Figure 48.

No.	1	2	3	4	5	Pure Cu
RD step barrier (eV)	0.45	0.47	0.45	0.48	0.49	0.62

Supplementary Information Table S2 | The reaction energies in the rate-determining step of C-C bond making on different configurations in the Supplementary Information Figure 49.



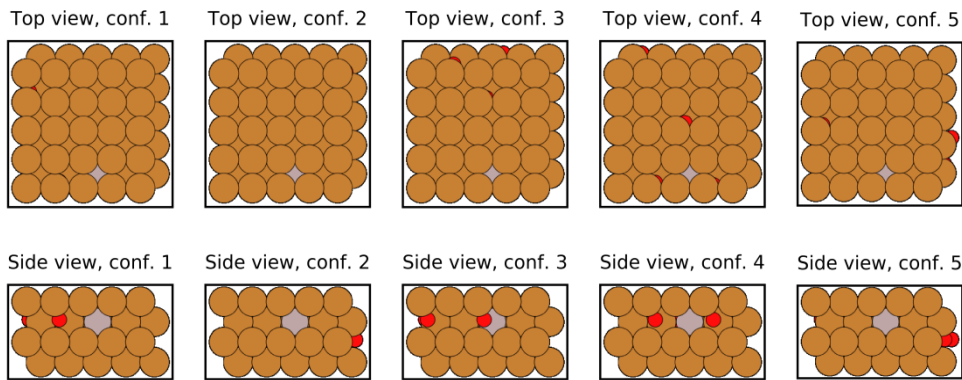
Supplementary Information Figure 50 | Models used to calculate the reaction energies in the rate-determining step of C-C bond making in the CO₂ reduction. 4% Al incorporated Cu (100) surface with different amounts of Cu-O bonds as shown in configurations 1-5.



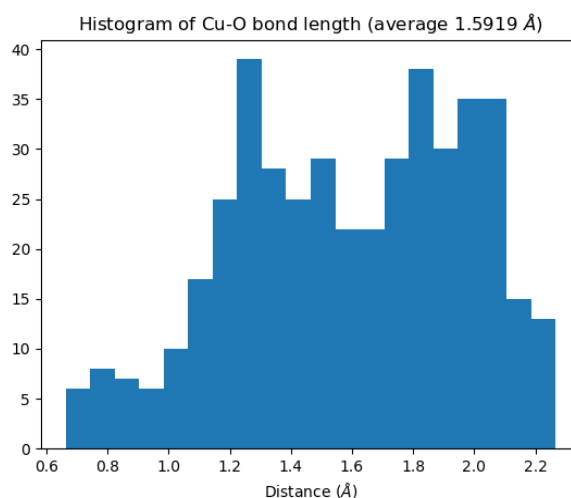
Supplementary Information Figure 51 | The distribution of Cu-O bond length in the Supplementary Information Figure 50.

No.	1	2	3	4	5	Pure Cu
RD step barrier (eV)	0.53	0.57	0.59	0.51	0.6	0.62

Supplementary Information Table S3 | The reaction energies in the rate-determining step of C-C bond making on different configurations in the Supplementary Information Figure 51.



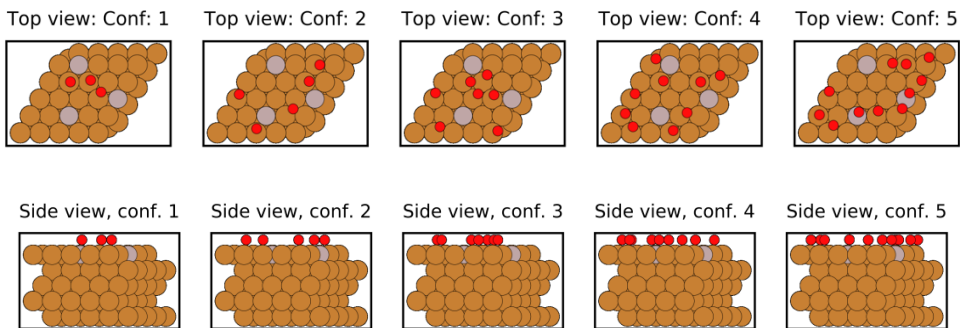
Supplementary Information Figure 52 | Models used to calculate the reaction energies in the rate-determining step of C-C bond making in the CO₂ reduction. 4% Al incorporated Cu (100) surface with different amounts of Cu-O bonds as shown in configurations 1-5.



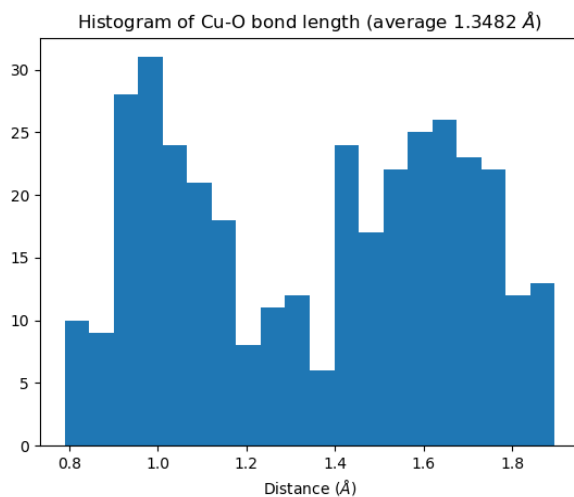
Supplementary Information Figure 53 | The distribution of Cu-O bond length in the Supplementary Information Figure 52.

No.	1	2	3	4	5	Pure Cu
RD step barrier (eV)	0.46	0.42	0.56	0.52	0.51	0.62

Supplementary Information Table S4 | The reaction energies in the rate-determining step of C-C bond making on different configurations in the Supplementary Information Figure 53.



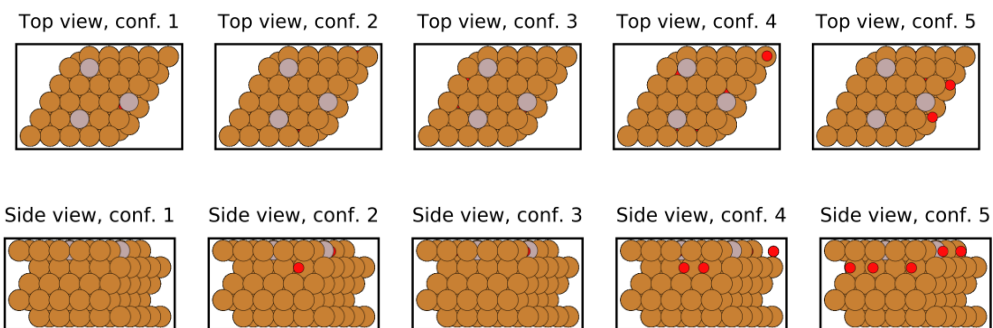
Supplementary Information Figure 54 | Models used to calculate the reaction energies in the rate-determining step of C-C bond making in the CO₂ reduction. 12% Al incorporated Cu (111) surface with different amounts of Cu-O bonds as shown in configurations 1-5.



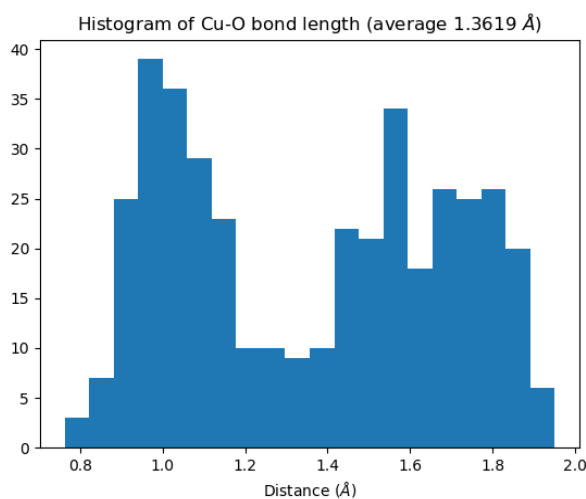
Supplementary Information Figure 55 | The distribution of Cu-O bond length in the Supplementary Information Figure 54.

No.	1	2	3	4	5	Pure Cu
RD step barrier (eV)	1.103	1.02	0.98	0.95	1.07	1.47

Supplementary Information Table S5 | The reaction energies in the rate-determining step of C-C bond making on different configurations in the Supplementary Information Figure 55.



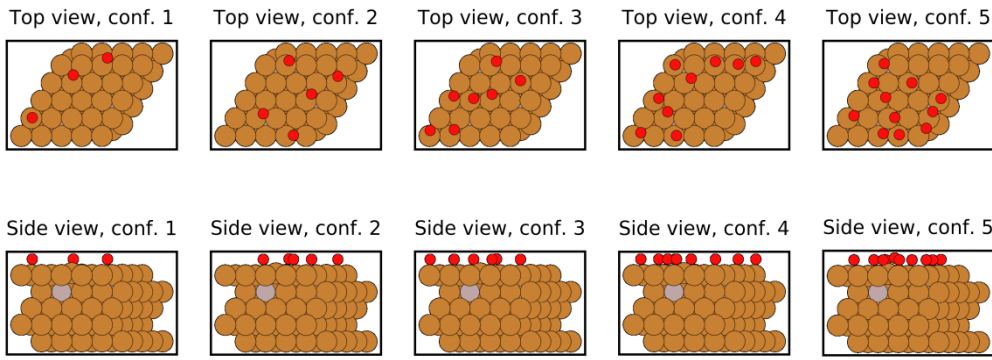
Supplementary Information Figure 56 | Models used to calculate the reaction energies in the rate-determining step of C-C bond making in the CO₂ reduction. 12% Al incorporated Cu (111) surface with different amounts of Cu-O bonds as shown in configurations 1-5.



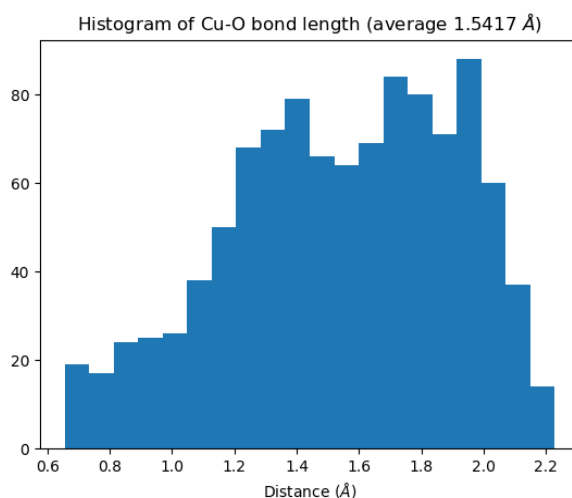
Supplementary Information Figure 57 | The distribution of Cu-O bond length in the Supplementary Information Figure 56.

No.	1	2	3	4	5	Pure Cu
RD step barrier (eV)	0.98	0.99	1.17	1.21	1.03	1.47

Supplementary Information Table S6 | The reaction energies in the rate-determining step of C-C bond making on different configurations in the Supplementary Information Figure 57.



Supplementary Information Figure 58 | Models used to calculate the reaction energies in the rate-determining step of C-C bond making in the CO₂ reduction. 12% Al incorporated Cu (111) surface with different amounts of Cu-O bonds as shown in configurations 1-5.

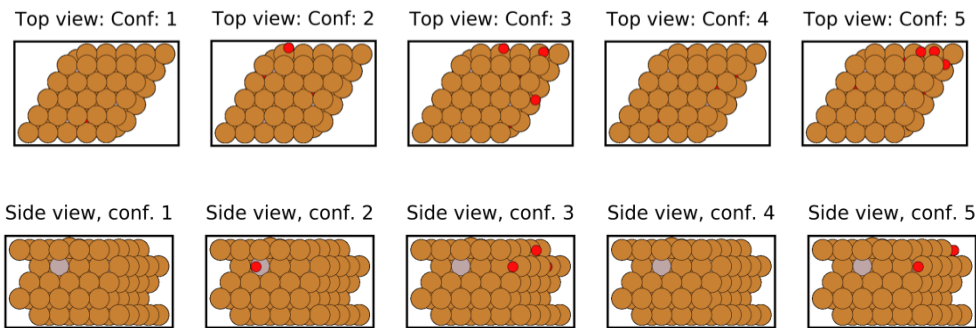


Supplementary Information Figure 59 | The distribution of Cu-O bond length in the rate-determining step of C-C bond making.

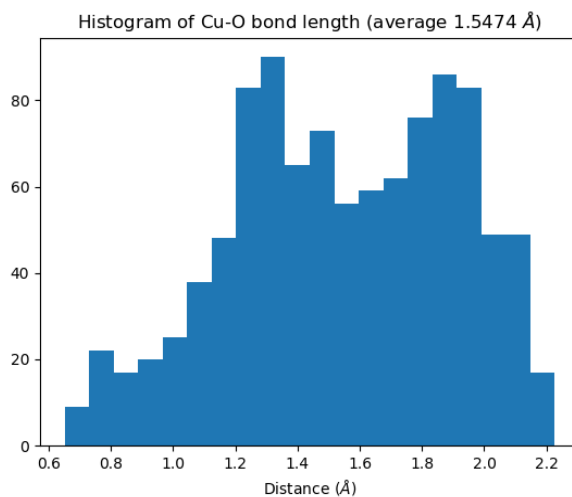
Supplementary Information Figure 58.

No.	1	2	3	4	5	Pure Cu
RD step barrier (eV)	0.92	1.03	1.03	1.10	1.13	1.47

Supplementary Information Table S7 | The reaction energies in the rate-determining step of C-C bond making on different configurations in the Supplementary Information Figure 59.



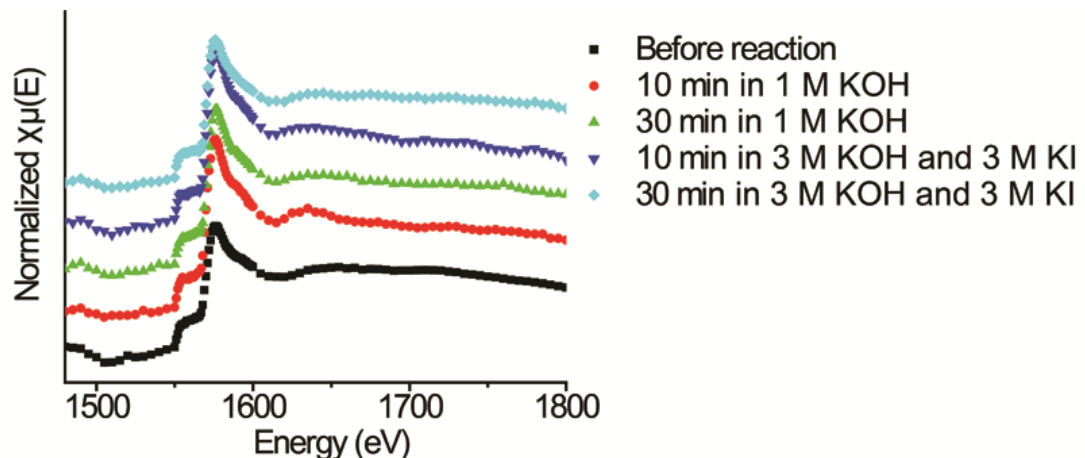
Supplementary Information Figure 60 | Models used to calculate the reaction energies in the rate-determining step of C-C bond making in the CO₂ reduction. 12% Al incorporated Cu (111) surface with different amounts of Cu-O bonds as shown in configurations 1-5.



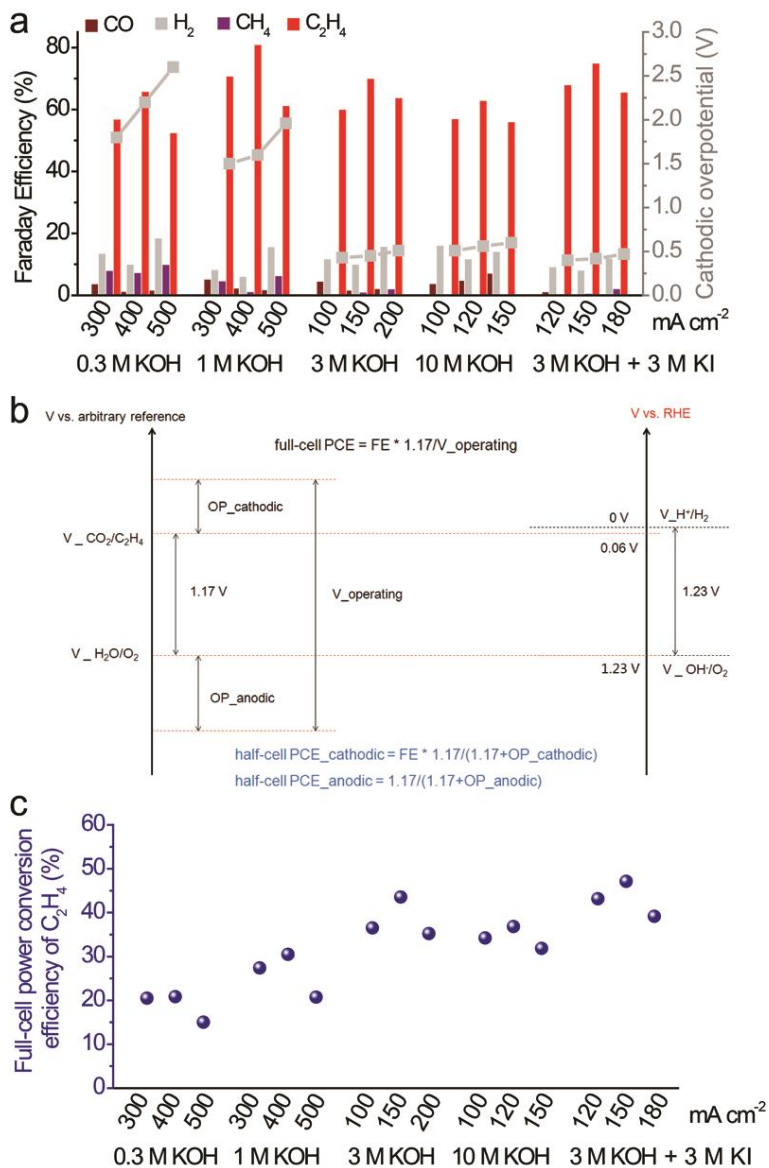
Supplementary Information Figure 61 | The distribution of Cu-O bond length in the Supplementary Information Figure 60.

No.	1	2	3	4	5	Pure Cu
RD step barrier (eV)	0.87	0.92	0.90	0.94	1.19	1.47

Supplementary Information Table S8 | The reaction energies in the rate-determining step of C-C bond making on different configurations in the Supplementary Information Figure 61.



Supplementary Information Figure 62 | X-ray absorption (XAS) spectra. XAS near-edge structure (XANES) spectra at the Al K-edge of de-alloyed Cu-Al catalyst before and right after 10, and 30 minutes of the CO₂ electroreduction reactions at 400 mA cm⁻² in 1 M KOH and 150 mA cm⁻² in 3 M KOH and KI.



Supplementary Information Figure 63 | CO₂ electroreduction performance on de-alloyed

Cu-Al/PTFE catalysts in alkaline electrolytes at different pH values. **a**, Faradaic efficiencies for gaseous products with its corresponding working potential of the de-alloyed Cu-Al catalysts in the different alkaline electrolytes and at different applied current densities.

b, Potential diagram for calculating the half-cell and full-cell PCEs. **c**, Calculated full-cell PCE of the Cu-Al catalyst when coupled with the best-in-class water oxidation reaction catalyst on the anode side^{S27}.

Note that anodic water oxidation and cathodic CO₂ reduction are two independent half reactions,

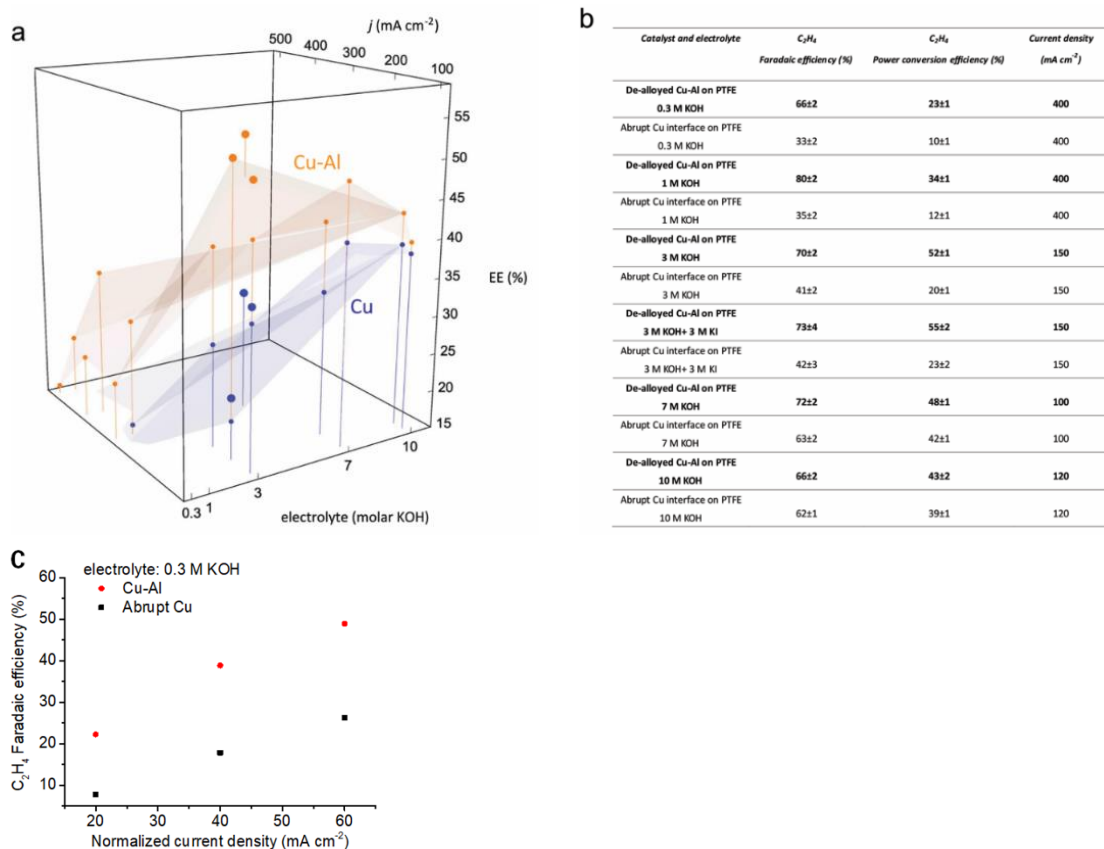
the half-cell cathodic PCE is thus important to quantify the performance on the cathodic side.

For example, it is difficult to compare which system is more efficient: 60% FE with 0.3 V OP and 62% FE with 0.32 VOP, or 60% FE with 0.3 V OP and 80% FE with 0.7 V OP at the same current density. Half-cell cathodic PCE combines OP and FE. It is straightforward to find out that the underlined are more efficient.

Moreover, the full-cell PCE can be calculated from the half-cell PCEs and FEs. As shown in the equations below , the full-cell PCE is: $PCE(f) = FE(c) \times FE(a) \times V_{theoretic} / (V_{theoretic} + OP_{cathodic} + OP_{anodic})$, the cathodic half-cell PCE is: $PCE(c) = FE(c) \times V_{theoretic} / (V_{theoretic} + OP_{cathodic})$, the anodic half-cell PCE is: $PCE(a) = FE(a) \times V_{theoretic} / (V_{theoretic} + OP_{anodic})$, where PCE (f, c, a) are full-cell, cathodic and anodic PCEs. FE(c, a) are cathodic and anodic FEs. OP_cathodic and OP_anodic are cathodic and anodic overpotentials. $V_{theoretic}$ is the theoretical potential for a redox reaction.

Therefore, $1/PCE(f) = 1/[FE(a) \times PCE(c)] + 1/[FE(c) \times PCE(a)] - 1/[FE(a) \times FE(c)]$.

In the electrochemical reduction of CO₂ to C₂H₄, the cathodic reaction is $2 CO_2 + 12 H^+ + 12 e^- \rightarrow C_2H_4 + 4 H_2O$, and the anodic reaction is $2 H_2O - 4 e^- \rightarrow O_2 + 4 H^+$. The theoretical potential $V_{theoretic} = 1.17$ V. The anodic FE for water oxidation is usually 100% because of no competing reactions. Thus, we would achieve a 47±1% full-cell C₂H₄ PCE when coupled with the best-in-class water oxidation reaction catalyst on the anode side^{S27}.



Supplementary Information Figure 64 | Performance comparison. **a**, the CO_2 -to- C_2H_4 PCE of the de-alloyed Cu-Al (pink) and Cu (blue). It is clear that the performance of Cu-Al is well above that of Cu under all the tested conditions. **b-c**, performance comparison of de-alloyed Cu-Al/PTFE vs. abrupt-interface Cu/PTFE under the same CO_2 -electroreduction conditions (**b**) and under kinetics-controlled conditions (**c**).

As shown in the comparison table above:

- In 1 M KOH, the de-alloyed Cu-Al achieves a high CO_2 -to- C_2H_4 Faradaic efficiency (FE) of $80\pm2\%$ at 400 mA cm^{-2} (ca. -1.5 V vs. RHE). In contrast, the abrupt-interface Cu shows a much lower C_2H_4 FE of $35\pm2\%$ under the same testing conditions.

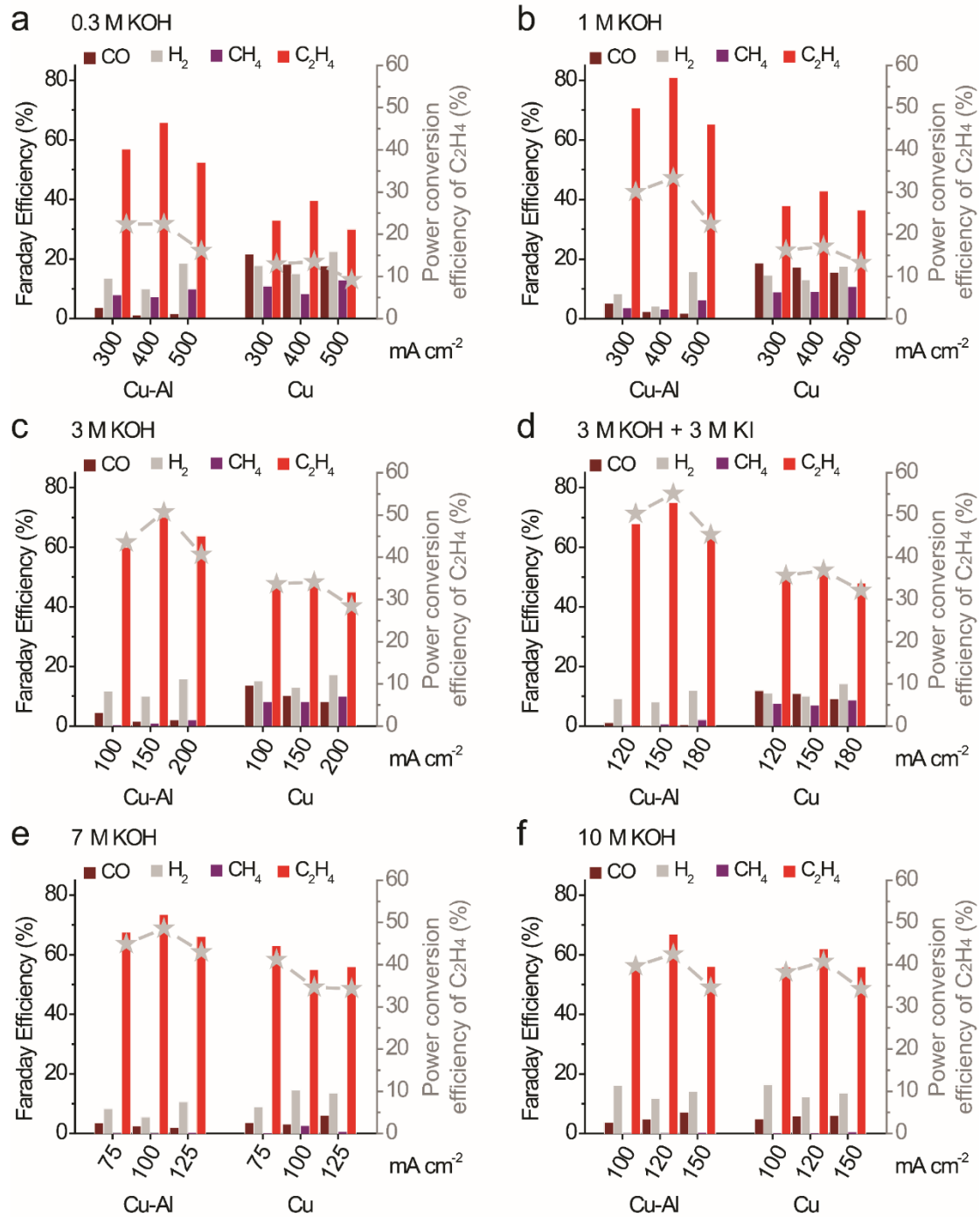
- In 3 M KOH + 3 M KI, the de-alloyed Cu-Al achieves an electricity-to-C₂H₄ half-cell power conversion efficiency (PCE) of 55±2% with a CO₂-to-C₂H₄ FE of 73±2% at a current density of 150 mA cm⁻² (ca. -0.4 V vs. RHE). In contrast, both the CO₂-to-C₂H₄ FE and PCE of the abrupt-interface Cu is substantially lower of 42±3% and 23±2%, respectively.
- In 3 M KOH, the de-alloyed Cu-Al realizes a CO₂-to-C₂H₄ FE of 70±2% and a half-cell PCE of 52±1%. It indicates that KI plays a modest role in performance enhancement.
- In 7-10 M KOH, the CO₂-to-C₂H₄ FE and PCE of the de-alloyed Cu-Al is also better than that of Cu, indicating that Cu-Al is superior under all the same conditions.

The improved C₂H₄ selectivity, from the previous best of 66% with the abrupt-interface Cu to the current record of 80±2%, is achieved through the successfully suppression of 1) the CO FE from the previous 7-8% to below 0.5%, owing to optimized CO adsorption energies on the Cu-Al surfaces near the top of both the activity and selectivity volcano plots for CO₂ reduction, and 2) the acetate FE from the previous 6% to below 1%, because we do not resort to using extremely high pH solution (10 M KOH) to promote C-C coupling, consequently the acetate by-production is reduced.

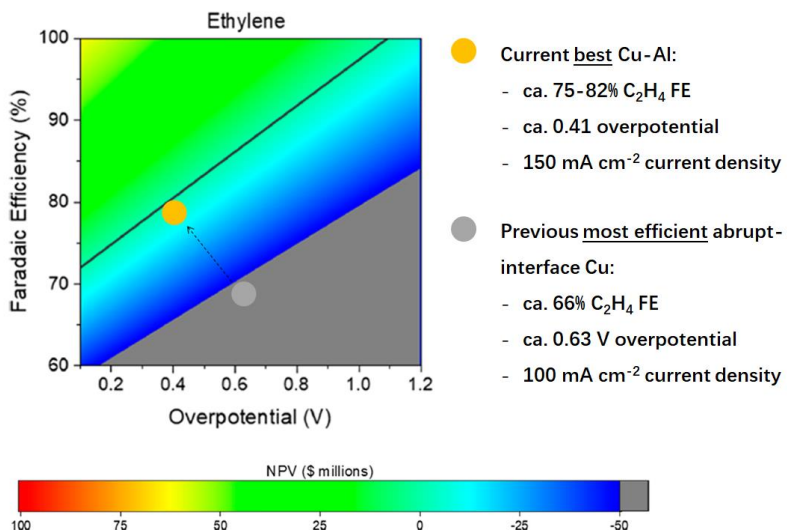
Note that the simultaneous increase in selectivity and current density are multiplicative. For example: assume we produce 1.00 kg/hr of C₂H₄ at 70% selectivity. If we increase selectivity to 80% with 50% increase in current density, we would yield [1 kg/hr × (0.8/0.7) × (1.5) = 1.71 kg/hr, a total 71% increase in the C₂H₄ productivity. The performance we obtained is potentially compatible with the current industry alkaline water splitting electrolyzer.

To compare the catalytic properties of Cu-Al and Cu under the kinetics-controlled conditions, we compared the activities of the samples at low current densities, staying far from the

diffusion-limited regime. We normalized the current density using measured electrochemically active surface areas (ECSAs). As seen in the Figure below, the C₂H₄ FE of Cu-Al is much higher than that of Cu in the low current density region, consistent with the high *intrinsic* activity of the Cu-Al catalyst in ethylene formation.

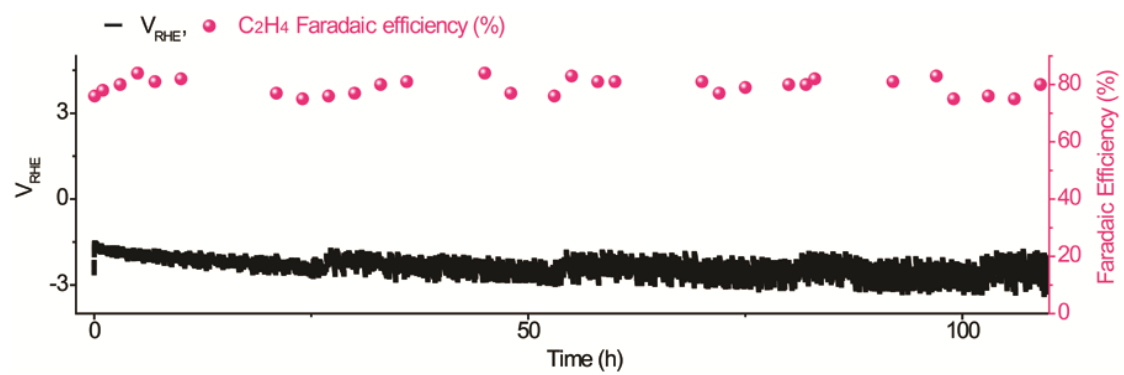


Supplementary Information Figure 65 | Products distribution. Products distribution of the de-alloyed Cu-Al/PTFE and abrupt-interface Cu/PTFE under the same CO₂-electroreduction conditions in Supplementary Information Figure 64.

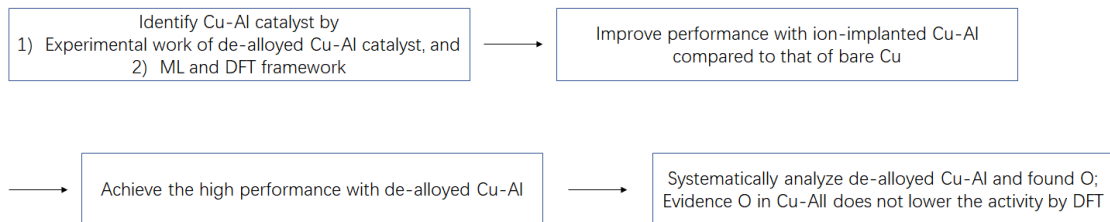


Supplementary Information Figure 66 | Techno-Economic Analysis. Techno-Economic Analysis of a generalized CO₂ electrolyzer with assumed C₂H₄ production of 100 tons/day (Figure 7 in Ref. S28): net present value vs. CO₂-to-C₂H₄ overpotential and selectivity under optimistic conditions. The solid line depicts the performance needed for an NPV of \$0. The performance of the Cu-Al in this work and reported abrupt-interface Cu is shown in the Figure when they are coupled with ideal anodes. "Reprinted with permission from (*Ind. Eng. Chem. Res.* 2018, 57, 2165-2177). Copyright (2019) American Chemical Society."

We plot in the Figure above the performance of the Cu-Al comparing with that of the previous most efficient abrupt-interface Cu in the Techno-Economic Analysis^{S28}, which estimates the net present value (NPV) of a generalized CO₂ electrolyzer system for C₂H₄ production at an assumed productivity of 100 tons/day with capital costs included. Under a clearly-stated set of assumptions, the energy advance obtained with the Cu-Al catalyst is capable of taking the cost of renewable ethylene production down into the break-even region. All prior reports, reside in the unprofitable regime. This is also the first example of high-order CO₂ electrolysis products, including ethylene, ethanol, propanol, acetate etc., showing an NPV close to the profitable region at a high current density over 100 mA cm⁻².



Supplementary Information Figure 67 | CO₂ electroreduction stability of the de-alloyed Cu-Al/PTFE electrode in a 1 M KOH electrolyte at an applied current density of 400 mA cm⁻².



Supplementary Information Figure 68 | Flow chat of this Cu-Al work.

Our timeline/workflow:

1. We experimentally evidence that Cu-Al is a superior electrocatalyst; we also used the machine-learning (ML) and density function theory (DFT) framework to screen a large space of materials, which is when we identified Cu-Al as a promising catalyst for CO₂ electroreduction.
2. Experimentally, we showed that incorporating 4-28% of Al on Cu surfaces by ion implantation increases the C₂H₄ Faradaic efficiency (FE) compared to pure Cu.
3. We scalably fabricate nanoporous Cu-Al with further improved C₂H₄ electroreduction performance.
4. We systematically analyzed the high-performance nanoporous Cu-Al catalyst, and found out that O was remained in the de-alloyed Cu-Al catalyst.
5. We used detailed, hand-performed (i.e., not automated) DFT calculations to confirm that the presence of O on the surface or in the subsurface of Cu-Al does not lower the surface activity of Cu-Al for CO₂ electroreduction.

Structure	E_ZPE(eV)	Cv_trans(0->T)(eV)	Cv_rot(0->T)(eV)	Cv_vib(0->T)(eV)	H(eV)
<i>Initial</i>	$2.17E+00$	$3.90E-02$	$3.90E-02$	$3.30E-01$	$2.61E+00$
<i>Final_a</i>	$2.62E+00$	$3.90E-02$	$3.90E-02$	$4.30E-01$	$3.16E+00$
<i>Final_b</i>	$2.15E+00$	$3.90E-02$	$3.90E-02$	$3.77E-01$	$2.63E+00$

Supplementary Information Table S9 | Zero-point energy and specific heat of different reactants, intermediates and products on the Al incorporated Cu (111) surface. It corresponds to the data used in Supplementary Information Figure 33.

Structure	S_trans(eV/K)	S_rot(eV/K)	S_vib(eV/K)	S(eV/K)	TS(eV)
<i>Initial</i>	2.19E-03	2.04E-03	2.08E-03	6.32E-03	1.88E+00
<i>Final_a</i>	2.19E-03	2.00E-03	2.78E-03	6.97E-03	2.08E+00
<i>Final_b</i>	2.19E-03	2.03E-03	6.68E-03	6.68E-03	1.99E+00

Supplementary Information Table S10 | Entropy and Gibbs free energy of different reactants, intermediates and products on the Al incorporated Cu (111) surface. It corresponds to the data used in Supplementary Information Figure 34.

<i>Structure</i>	E_ZPE(eV)	Cv_trans(0->T)(eV)	Cv_rot(0->T)(eV)	Cv_vib(0->T)(eV)	H(eV)
<i>Initial</i>	2.15E+00	3.90E-02	3.90E-02	1.88E-01	2.44E+00
<i>Final_a</i>	2.43E+00	3.90E-02	3.90E-02	1.82E-01	2.71E+00
<i>Final_b</i>	1.97E+00	3.90E-02	3.90E-02	1.76E-01	2.25E+00

Supplementary Information Table S11 | Zero-point energy and specific heat of different reactants, intermediates and products on the Al incorporated Cu (100) surface. It corresponds to the data used in Supplementary Information Figure 35.

Reference

- S1. Jain, A. *et al.* *APL Materials* **1**, 1-11 (2013).
- S2. Hjorth Larsen, A. *et al.* *J. Phys. Condens. Matter* **29**, 273002 (2017).
- S3. Ong, S. P. *et al.* *Comp. Mater. Sci.* **68**, 314-319 (2013).
- S4. Kresse, G. & Hafner, J. *Phys. Rev. B* **47**, 558-561 (1993).
- S5. Kresse, G. & Hafner, J. *Phys. Rev. B* **49**, 14251-14269 (1994).
- S6. Kresse, G. & Furthmüller, J. *Comp. Mater. Sci.* **6**, 15-50 (1996).
- S7. Kresse, G. & Furthmüller, J. *Phys. Rev. B* **54**, 11169-11186 (1996).
- S8. Bernhardsson, E. & Freider, E. *Luigi, a Python package that builds complex pipelines of batch jobs* (2012).
- S9. Jain, A. *et al.* *Concurr Comp-Pract E* **22**, 685-701 (2010).
- S10. Olson, R. S. *et al.* In *Proc. of the European Conference on the Applications of Evolutionary Computation*. Springer International Publishing 123-137 (2016).
- S11. Hammer, B., Hansen, L. B. & Nørskov, J. *Phys. Rev. B* **59**, 7413-7421 (1999).
- S12. Nørskov, J. K., Studt, F., Abild-Pedersen, F. & Bligaard, T. *Angew. Chem. In. Ed.* **54**, 10404-10405 (2015).
- S13. Liu, X. *et al.* *Nat. Commun.* **8**, 15438 (2017).
- S14. Studt, F. *et al.* *Catal. Lett.* **143**, 71-73 (2013).
- S15. Abild-Pedersen, F. & Andersson, M. P. *Surf. Sci.* **601**, 1747-1753 (2007).
- S16. Wellendorff, J. *et al.* *Phys. Rev. B* **85**, 32-34 (2012).
- S17. Tran, K. & Ulissi, Z. Active learning across intermetallics to guide discovery of electrocatalysts for CO₂ reduction and H₂ evolution. *Nat. Catalysis.* **1**, 696–703 (2018).

- S18. Pedregosa, F. *et al.* *J. Mach. Learn. Res.* **12**, 2825-2830 (2012).
- S19. van der Maaten, L. 15, 3221-3245 (2014).
- S20. Blöchl, P. E. *Phys. Rev. B* **50**, 17953 (1994).
- S21. Kresse, G. & Joubert, D. *Phys. Rev. B* **59**, 1758 (1999).
- S22. Kresse, G. & Furthmüller, *Phys. Rev. B* **54**, 11169 (1996).
- S23. Perdew, J. P., Burke, K. & Ernzerhof, M. *Phys. Rev. Lett.* **77**, 3865 (1996).
- S24. Larsen, A. H. *et al.* *J. Phys. Condens. Matter* **29**, 273002 (2017).
- S25. Monkhorst, H. J. & Pack, J. D. *Phys. Rev. B* **13**, 5188 (1976).
- S26. Xiao, H. *et al.* *J. Am. Chem. Soc.* **139**, 130-136 (2017).
- S27. Zhang, B. *et al.* *Science* **352**, 6238 (2016).
- S28. Jouny, M. *et al.* *Systems. Ind. Eng. Chem. Res.* **57**, 2165 (2018).